

## Research Paper

# Fast physically-based probabilistic modelling of rainfall-induced shallow landslide susceptibility at the regional scale considering geotechnical uncertainties and different hydrological conditions

Hongzhi Cui <sup>a,b</sup>, Vicente Medina <sup>b</sup>, Marcel Hürlimann <sup>b</sup>, Jian Ji <sup>a,c,\*</sup>

<sup>a</sup> Geotechnical Research Institute, Hohai University, Nanjing, China

<sup>b</sup> Division of Geotechnical Engineering and Geosciences, Department of Civil and Environmental Engineering, Universitat Politècnica de Catalunya, Barcelona, Spain

<sup>c</sup> Department of Civil Engineering, Monash University, Clayton, VIC, Australia

## ARTICLE INFO

**Keywords:**

Landslide susceptibility assessment  
Hydrological conditions  
Physically-based probabilistic modelling  
First-order reliability method  
Cross-negative-correlation

## ABSTRACT

The inherent uncertainty in hydro-geotechnical parameters presents a significant challenge for accurately predicting rainfall-triggered shallow landslides in mountainous regions. In this study, a novel probabilistic framework was developed and implemented in the “Py.GIS-FSLAM-FORM” software, designed to address the complexities associated with parameter uncertainty, correlation, and distribution. By combining the Fast Shallow Landslide Assessment Model (FSLAM) with the First-Order Reliability Method (FORM), we have enhanced the traditional probabilistic approach to create more accurate landslide susceptibility maps. This study emphasizes the uncertainty of geotechnical parameters and the critical influence of hydrological conditions on landslide susceptibility, especially focusing on the interaction between antecedent recharge ( $q_a$ ) and event rainfall ( $P_e$ ). In our study area (Val d’Aran, Spain), the probabilistically based results revealed that areas of very high susceptibility are significantly affected by event rainfall, particularly on slopes of 30–40 degrees and aspects between 100 and 250 degrees. The variability in geotechnical parameters, especially the coefficient of variation (COV) in cohesion and friction angle, plays a crucial role in landslide susceptibility assessment, with increased COVs leading to greater landslide uncertainty. Additionally, cross-negative correlations and non-normal distributions of geotechnical parameters substantially influence the spatial distribution of landslides, notably when combining antecedent recharge with event rainfall. These results highlight the importance of incorporating parameter variability and hydrological conditions in susceptibility models to improve the precision of regional landslide forecasts. While the study was performed in Val d’Aran, its methodologies and conclusions are relevant to mountainous areas worldwide, offering insights for refining landslide prediction models and susceptibility assessments, contributing to global efforts in landslide disaster prevention.

## 1. Introduction

Landslides are one of the most common and significant geological hazards in natural terrains, and rainfall plays a crucial role in triggering and exacerbating landslide events (Mondini et al., 2023). In particular, shallow landslides are often observed as the primary impacting phenomenon at the regional scale and they can lead to considerable losses. As a result, conducting appropriate landslide susceptibility, hazard and risk management is a significant responsibility of stakeholders and relevant government departments (Zieher et al., 2017).

Physically-based models are considered to be a powerful tool for assessing the susceptibility of rainfall-triggered shallow landslides

which can simulate the hydrological and mechanical processes of landslides (Corominas et al., 2014). The factor of safety (FS) is typically determined in this method by considering the failure mechanism, the geometry of the failure surface, variations in rainfall infiltration, and associated pore water pressure within the slope at a specific pixel size (Durmaz et al., 2023). The analysis not only facilitates the comprehension of the physical conditions that contributed to previous failures but also enables the prediction of future changes, such as climate, land use and land cover (Hürlimann et al., 2022).

Rainfall-induced landslide physical models primarily rely on the slope-parallel lateral flow (Montgomery and Dietrich, 1994; Pack et al., 1998), vertical (Baum et al., 2008; Cui et al., 2024; Montrasio and

\* Corresponding author at: Geotechnical Research Institute, Hohai University, 210024 Nanjing, China.

E-mail addresses: [marcel.huerlimann@upc.edu](mailto:marcel.huerlimann@upc.edu) (M. Hürlimann), [ji0003an@e.ntu.edu.sg](mailto:ji0003an@e.ntu.edu.sg) (J. Ji).

Valentino, 2008), or their combination (Medina et al., 2021). However, to estimate slope stability, most of the proposed physically-based models are mainly considering coupling hydrological models with the infinite slope (Carrara et al., 2008; Meisina and Scarabelli, 2007; Segoni et al., 2012; Zhang et al., 2016). The calculation of the FS for each soil column may be underestimated if the stability of adjacent soil columns is not considered. Consequently, three-dimensional limit equilibrium methods have also been employed for regional landslide assessment (Ho and Lee, 2016; Jiang et al., 2023; Oguz et al., 2022). Although the literature has demonstrated that three-dimensional models yield higher accuracy compared to two-dimensional infinite slope methods based on limit equilibrium (Chen et al., 2023; Tran et al., 2018), their computational time and resource requirements are inevitably greater. Therefore, the utilisation of a two-dimensional infinite slope model in conjunction with hydrological analysis remains the predominant approach for forecasting rainfall-triggered landslides at the regional scale (Raimondi et al., 2023). Recently, Medina et al. (2021) proposed a novel physically-based approach called FSLAM to efficiently assess shallow landslides by incorporating both vertical and horizontal flow. The proposed model not only considers the influence of antecedent rainfall but also enables the simulation of slope stability under event rainfall.

The issue of parameter uncertainty stands out as a prominent challenge encountered by physically-based models, which merits careful consideration (Ji et al., 2022). Deterministic analysis methods are commonly employed in geotechnical engineering practice to evaluate slope stability (Liu and Wu, 2008). However, it should be noted that this analytical method is an idealized approach, as the acquisition of accurate and appropriate soil parameters necessitates a comprehensive site investigation and meticulous laboratory testing (Shinoda et al., 2019; Tandjiria et al., 2000; Tao et al., 2023; Zieher et al., 2017). To obtain representative parameter values, a comprehensive analysis is imperative. However, in practical applications, the majority of soil layer parameters are determined through interpolation/extrapolation methods based on limited field and laboratory data (Park et al., 2019). The determination of soil parameters relies heavily on empirical correlations and expert criteria, thereby introducing a heightened level of uncertainty in the estimation of soil properties.

Moreover, the inherent variability of the soil as well as the spatial variability of soil thickness makes it exceedingly challenging to gather comprehensive data across a vast area, thereby rendering parameter uncertainty inevitable (Liu et al., 2018; Weidner et al., 2018; Zhang et al., 2014). These uncertainties pose significant challenges in accurately predicting the spatial and temporal distribution of rainfall-induced shallow landslides. Failing to consider uncertainties and exclusively depending on deterministic values for model parameters can lead to estimations that are either unrealistic or excessively conservative (Raia et al., 2014). For instance, field investigations have demonstrated significant spatial variations in soil cohesion and friction angle, which are crucial factors influencing slope deformation (Wang et al., 2020). In addition to the inherent uncertainty associated with geotechnical and hydrological parameters (Aleotti and Chowdhury, 1999), various sources contribute to uncertainties in landslide susceptibility assessment (Bui et al., 2016; Pradhan, 2013). These include initial hydrological conditions (Bozzolan et al., 2023) and soil layer heterogeneity (Oguz et al., 2022) which demonstrated its significant impact on slope stability, and reported uncertainties arising from GIS data sources (Huang et al., 2023), DEM resolution (Fuchs et al., 2014), and sample size (Yi et al., 2020).

Regarding all these aspects, probabilistic methods are regarded as a more appropriate tool due to their ability for addressing uncertainties through the utilisation of probabilistic models, wherein parameter's uncertainty is defined using probability density functions (Durmaz et al., 2023; Ji et al., 2019). Some of the models employ analytical solutions to determine the PDF of FS, assuming that cohesion and friction angle follow a normal distribution (Medina et al., 2021). Nevertheless, others utilise Monte Carlo simulation (MCS) techniques to address parameter

uncertainties involve calibrating model parameters through multiple simulations (Li et al., 2022; Park et al., 2019; Wang et al., 2023). In the latter case, the model performance is assessed by varying parameter values and selecting the optimal ones for generating susceptibility maps. It is worth noting that achieving comprehensive calibration necessitates computationally intensive multiple simulations (Gorsevski et al., 2006; Gupta et al., 2023; Marin and Mattos, 2020).

However, the implementation of MCS-based calibration strategies is prohibitively time-consuming, particularly for models requiring rapid simulation periods. This approach becomes especially impractical when conducting fast assessments of landslides over larger geographical areas. Furthermore, the potentially unrealistic nature of certain input data such as regional or medium-scale soil thickness and spatial distribution as well as mapping of soil layer material properties have been highlighted in recent publications (Doljan et al., 2021). Hence, there persists a need for more pragmatic and less time-intensive probabilistic methods to facilitate susceptibility assessment through physical models in areas with scarce data availability. In light of this consideration, the first-order reliability method emerges as a viable choice due to its rapid convergence rate and high computational accuracy (Ji and Kodikara, 2015). Additionally, the uncertainty of model parameters encompasses not only their variability but also necessitates consideration of parameter correlations (Hwang et al., 2023; Javankhoshdel and Bathurst, 2016; Low and Phoon, 2015). Neglecting the correlation between parameters and treating model parameters as independent and unrelated may result in an overestimation of failure probability when considering individual slopes (Wang et al., 2020). The detailed investigation of how the correlation between geological parameters, such as cohesion and friction angle, influences the susceptibility of regional shallow landslides remains a research topic that warrants consideration in physical models at a regional scale.

In conclusion, despite advancements in related research, existing landslide susceptibility models face challenges in accurately simulating the uncertainty of physical parameters. Numerous regional-scale physically-based probabilistic models encounter challenges in achieving a balance among variability, cross-correlation, and computational efficiency of probabilistic parameters, which are crucial factors for the rapid prediction of shallow landslides. Conversely, while MCS and other similar probabilistic methods efficiently address parameter uncertainty, their computational demands impose practical limitations on the application of regional probabilistic landslide susceptibility analysis. Additionally, a comprehensive consideration of hydrological factors is critical for enhancing the accuracy of rainfall-triggered landslide susceptibility models as well.

This study aims to assess how uncertainties in model parameters, including their variability and correlation, affect the prediction of shallow landslide susceptibility under different hydrological conditions. This includes considering the effects of antecedent recharge and event rainfall conditions. First, we couple the Fast Shallow Landslide Assessment Model (FSLAM) with the First-Order Reliability Method (FORM). This integration provides a physically-based probabilistic framework for regional landslide assessment, incorporating uncertainties in geological and hydrological parameters. Second, through a case study in Val d'Aran (Pyrenees, Spain), we examine susceptibility maps affected by different coefficients of variation (COV), aiming to assess the model's sensitivity to parameter variability in various hydrological conditions. Following this, the study explores the effects of statistical correlation and non-normal distribution on landslide susceptibility. It focuses on understanding how cross-correlation and non-normal distributions of soil shear strength parameters, coupled with hydrological factors like antecedent recharge and event rainfall, influence the spatial distribution of landslide probability. All analyses were conducted using the Py.GIS-FSLAM-FORM v1.0 software, which is specifically created for this study.

## 2. Methodology

### 2.1. FSLAM model for rainfall-induced shallow landslide prediction

#### 2.1.1. The infinite slope stability model

For shallow landslide analysis, the infinite slope stability model has been well-recognized by geotechnical researchers. Considering a groundwater table exists parallel to the slope surface, the factor of safety can be calculated by Lambe and Whitman (1979) and Pack et al. (1998):

$$FS = \frac{C}{g\rho_s z \cos\theta \sin\theta} + \left(1 - \left(\frac{h}{z}\right)\left(\frac{\rho_w}{\rho_s}\right)\right) \left(\frac{\tan\varphi}{\tan\theta}\right) \quad (1)$$

where  $g(m/s^2) = 9.8$  is the gravity,  $\rho_s (\text{kg/m}^3)$  is the density of saturated soils,  $\rho_w (\text{kg/m}^3)$  is the density of water,  $\theta (^{\circ})$  is the terrain slope,  $h (\text{m})$  and  $z (\text{m})$  are respectively the water table depth and sliding soil depth,  $\varphi (^{\circ})$  denotes internal friction angle of the soil shear strength, and  $C (\text{kPa})$  denotes total cohesion of the soil shear strength, which is composed of the effective cohesion  $C_s (\text{kPa})$ , and root cohesion  $C_r (\text{kPa})$ , such that

$$C = C_s + C_r \quad (2)$$

#### 2.1.2. Hydrological modelling

In rainfall infiltration conditions, the stability of surficial soil slopes is significantly influenced by the changing groundwater table, i.e., the value of  $h$  in Eq. (1). The hydrological model incorporating two different water flow mechanisms (lateral flow and vertical flow) was proposed in the FSLAM model (Medina et al., 2021). In brief, the mid-long-term impact of rainfall on the water table ( $h_a (\text{m})$ ) associated with the antecedent precipitation ( $q_a (\text{mm/d})$ ) is characterized by the lateral flow, and the short-term influence of rainfall on the water table ( $h_e (\text{m})$ ) related to specific event rainfall ( $P_e (\text{mm/d})$ ) is represented by the vertical flow. As a result of the rainfall infiltration, the final depth of the groundwater table ( $h (\text{m})$ ) can be evaluated by (see Fig. 1)

$$h = h_a + h_e \quad (3)$$

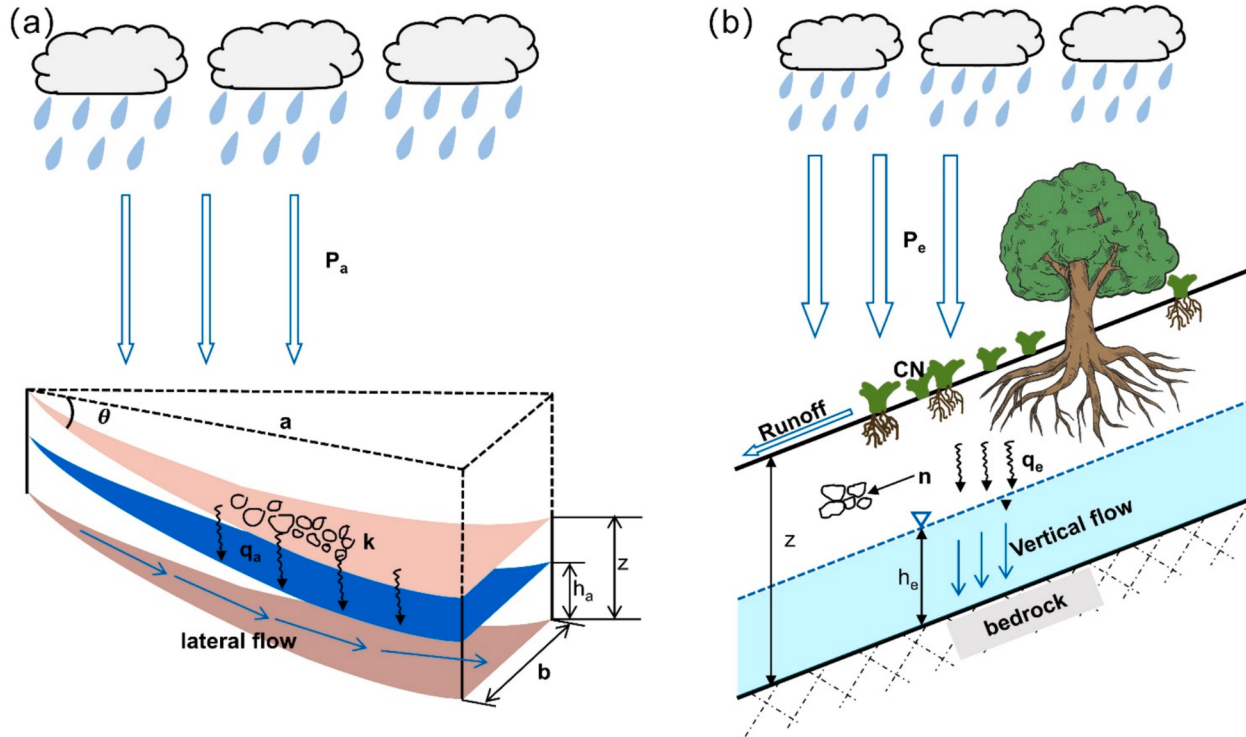


**Fig. 1.** Hydrological model incorporated in FSLAM (Adapted from Medina et al. (2021)): (a) Antecedent rainfall ( $P_a$ ) and effective antecedent recharge ( $q_a$ ) with lateral flow approach; (b) Event rainfall ( $P_e$ ) with vertical flow approach.

It should be noted that the lateral flow is primarily assessed by considering the variation of the groundwater table due to the recharge of antecedent rainfall in the FLSAM model, i.e.,  $h_a$ . In this paper, the model of  $h_a$  proposed by Montgomery and Dietrich (1994) is adopted:

$$h_a = \left(\frac{a}{b}\right) \frac{q_a}{K \sin\theta \cos\theta} \left(\frac{\rho_w}{\rho_s}\right) \quad (4)$$

where  $a (\text{m}^2)$  is the drainage area,  $b (\text{m})$  is the cell size,  $K (\text{m/s})$  is the saturated hydraulic conductivity of soil and  $q_a (\text{mm/d})$  is the effective antecedent water recharge (Medina et al., 2021).

On medium to long time scales (typically months), the effective recharge ( $q_a$ ) that infiltrates into the soil layer can be estimated from the adjusted antecedent effective rainfall ( $P_a$ , unit: mm). It is important to note that the  $P_a$  mentioned here is not equivalent to the total rainfall observed, as the total rainfall also includes the fraction that fails to infiltrate, such as losses from runoff and evaporation. Therefore, it is crucial to accurately assess the effective rainfall based on water balance theory within a given study area (Medina et al., 2021). However, as the FSLAM model does not include a water balance algorithm, it is necessary for the user to determine the long-term effective antecedent water recharge (mm/d) by external software or modelling, such as EasyBal model (Abancó et al., 2024).

Meanwhile, the variation of groundwater table related to the event rainfall into porous soils in the FSLAM model, i.e.,  $h_e$ , is calculated by:

$$h_e = \frac{q_e}{n} \quad (5)$$

where  $q_e$  is the storm event infiltration, and  $n$  is the soil porosity.

To estimate the value of  $q_e$ , the SCS-CN model (USDA, 1986) is adopted by converting the event rainfall ( $P_e$ ) into groundwater recharge, which is written by

$$q_e = P_e - \frac{(P_e - (5080/CN - 51))^2}{P_e + 4 \cdot (5080/CN - 51)} \quad (6)$$

3

Therefore,  $h_e$  can be further formatted as follows:

$$h_e = \frac{P_e}{n} - \frac{[P_e - (5080/CN - 51)]^2}{n[P_e + 4 \cdot (5080/CN - 51)]} \quad (7)$$

Considering the above-mentioned hydrological model for rainfall infiltration, the generic formula to calculate FS in the FSLAM model is expressed as follows:

$$FS = \frac{C}{gp_s z \cos \theta \sin \theta} + \left( 1 - \left( \left( \frac{a}{b} \right) \frac{q_a}{Kz \sin \theta \cos \theta} + \frac{q_e}{n \cdot z} \right) \left( \frac{\rho_w}{\rho_s} \right) \right) \left( \frac{\tan \varphi}{\tan \theta} \right) \quad (8)$$

## 2.2. Fast computation of landslide probability using FORM with HLRF-x recursive algorithm

For a given input data set, the computation of FS using Eq. (8) can be very fast, thus making it possible for regional landslide prediction with consideration of rainfall infiltration mechanisms. However, the model input parameters are by no means deterministically available at a regional scale. The probabilistic analysis is therefore a more rational approach to conducting regional landslide predictions. Mathematically, the physical model in terms of FS-based FSLAM can be extended into the probabilistic description, such that:

$$P_f = \int_{g(\mathbf{x}) < 0} f(\mathbf{x}) d\mathbf{x} \quad \text{with limit state function (LSF): } g(\mathbf{x}) = FS(\mathbf{x}) - 1 \quad (9)$$

where the vector  $\mathbf{x} = (C, \tan \varphi, K, q_a, q_e, \dots)$  denoting a collection of random variables (of input parameters),  $f(\mathbf{x})$  is the joint probability distribution function of random variables  $\mathbf{x}$ , and  $FS(\mathbf{x})$  is a functional format of Eq. (8).

This integral equation for  $P_f$  is nearly impossible to solve at speed, not to mention for regional landslide analysis. Alternatively, an efficient approximate solution known as the first-order reliability method (FORM) can be adopted, which has the following necessary recipes:

$$P_f = \Phi(-\beta_f) \quad (10)$$

$$\beta_f = \sqrt{\left[ \frac{\mathbf{x}_i^* - u_i^N}{\sigma_i^N} \right]^T \mathbf{R}^{-1} \left[ \frac{\mathbf{x}_i^* - u_i^N}{\sigma_i^N} \right]} \quad (11)$$

where  $\Phi(\cdot)$  denotes the standard normal cumulative distribution function,  $\beta_f$  is called the reliability index,  $\mathbf{x}_i^*$  denotes the most probable failure point (MPP) value of  $i$ th random variable (denoted in terms of random variable  $\mathbf{x}$ ),  $u_i^N$  and  $\sigma_i^N$  denote the equivalent normal mean and standard deviation of the  $i$ th variable, respectively, and they contain important information on  $\mathbf{x}$ 's semi-probability distribution functions,  $\mathbf{R}$  is the correlation matrix of all random variables. A detailed explanation can be found in Low and Tang (2007).

FORM is a semi-probability calculation method that is well-known in geotechnical engineering failure analysis. The fundamental concept of the FORM probabilistic calculation is to find the reliability index (RI) evaluated at the MPP'  $\mathbf{x}$  values. In this work, we adopt the fast recursive algorithm HLRF-x proposed by Ji and Kodikara (2015) to implement the FORM calculation into GIS. In brief, the HLRF-x recursive algorithm for locating the MPP in the space of random variables defined by vector  $\mathbf{x}$  ( $\mathbf{x}$ -space) is written as follows:

$$\mathbf{x}_{k+1} = \boldsymbol{\mu}_k^N + \frac{1}{\nabla g(\mathbf{x}_k)^T \mathbf{T}_k \nabla g(\mathbf{x}_k)} [\nabla g(\mathbf{x}_k)^T (\mathbf{x}_k - \boldsymbol{\mu}_k^N) - g(\mathbf{x}_k)] \mathbf{T}_k \nabla g(\mathbf{x}_k) \quad (12)$$

where  $\mathbf{T}_k = [\sigma_k^N]^T \mathbf{R} [\sigma_k^N]$  is the transformation matrix,  $\mathbf{x}_k$  is the vector of random variables in  $x$ -space, and  $\boldsymbol{\mu}_k^N$  is the vector of equivalent MV to convert random variables into the normal distribution. Further, the

diagonal matrix  $\begin{bmatrix} \sigma_{k,i}^N & \cdots & 0 \\ \vdots & \sigma_{k,n}^N & \vdots \\ 0 & \cdots & \sigma_{k,m}^N \end{bmatrix}$ ,  $\sigma_{k,i}^N$  is the equivalent normal stand-

dard deviation of the  $i$ th random variables evaluated at  $\mathbf{x}_k$ .  $\nabla g(\mathbf{x}_k)$  denotes the gradient vectors of the LSF evaluated at  $\mathbf{x}_k$ .

Furthermore, regarding the probabilistic analysis, outcomes are anchored in the FSLAM framework, amalgamated with the FORM-based HLRF\_x algorithm. The choice of a threshold, specifically referring to the probability of failure (POF), plays a pivotal role in assessing landslide susceptibility. Adopting the criteria delineated by Lacasse and Nadim (2011), susceptibility levels were categorized as follows: I (very low) with  $POF \leq 0.01$ ; II (low) for  $0.01 < POF \leq 0.1$ ; III (moderate) for  $0.1 < POF \leq 0.5$ ; IV (high) when  $0.5 < POF \leq 0.9$ ; and V (very high) when  $POF > 0.9$ .

## 2.3. Brief description of Py.GIS-FSLAM-FORM v1.0

### 2.3.1. General overview

Implementation of the FORM-based regional landslide probability analysis in the GIS platform has various challenges, which are not encountered in other uncertainty propagation methods, for example, FOSM, MCs, and stochastic methods (Medina et al., 2021). One such challenge is the computational intensity for implementing the recursive algorithm HLRF\_x, which involves several iterative calculations for each of the  $P_f$  outputs. The standard grid-based computation in popular GIS-related software such as QGIS will not work for FORM. To solve those involved challenges, we developed a Windows-based software that provides a user-friendly execution to perform the regional landslide susceptibility mapping, called "Py.GIS-FSLAM-FORM v1.0". Fig. 2 shows the computational workflow of this software, and the main steps are summarised as follows:

- (1) Input the required files for building the basic geospatial dataset (i.e., *input dataset*);
- (2) Select the desired output files for slope stability modelling (*landslide physical model*);
- (3) Perform the physically-based landslide probability evaluations using *FSLAM-FORM* modules;
- (4) Generate the outcome maps in the form of raster layers (i.e. *output results*).

Regarding the FSLAM stability modelling, the program principally confirms three conditions including: (i) preliminary stability, (ii) initial stability considering the effective antecedent recharge ( $q_a$ ), as well as (iii) final stability after event rainfall( $q_a + P_e$ ).

### 2.3.2. Computation efficiency

As an example, in the Val d'Aran region, the raster results files were generated at a resolution of 5 m × 5 m, resulting in approximately 13 million cells. Simulations conducted using GIS-FSLAM-FORM demonstrated a total runtime of fewer than 20 min, encompassing both modelling calculations and result generation. It is important to note that the efficiency of probabilistic analysis employing FORM with the HLRF\_x algorithm necessitates iterative improvements within this framework. This further enhances the applicability of the FORM reliability method for rapid assessment of landslide susceptibility on a large scale.

### 2.3.3. Evaluation of model forecasting accuracy

The performance of the probabilistic model is investigated, focusing on two main aspects. Firstly, we employed the widely recognized Receiver Operating Characteristic (ROC) analysis and the corresponding Area Under the Curve (AUC) (Wei et al., 2021). The ROC curve plots the False Positive Rate (FPR) and True Positive Rate (TPR) at different

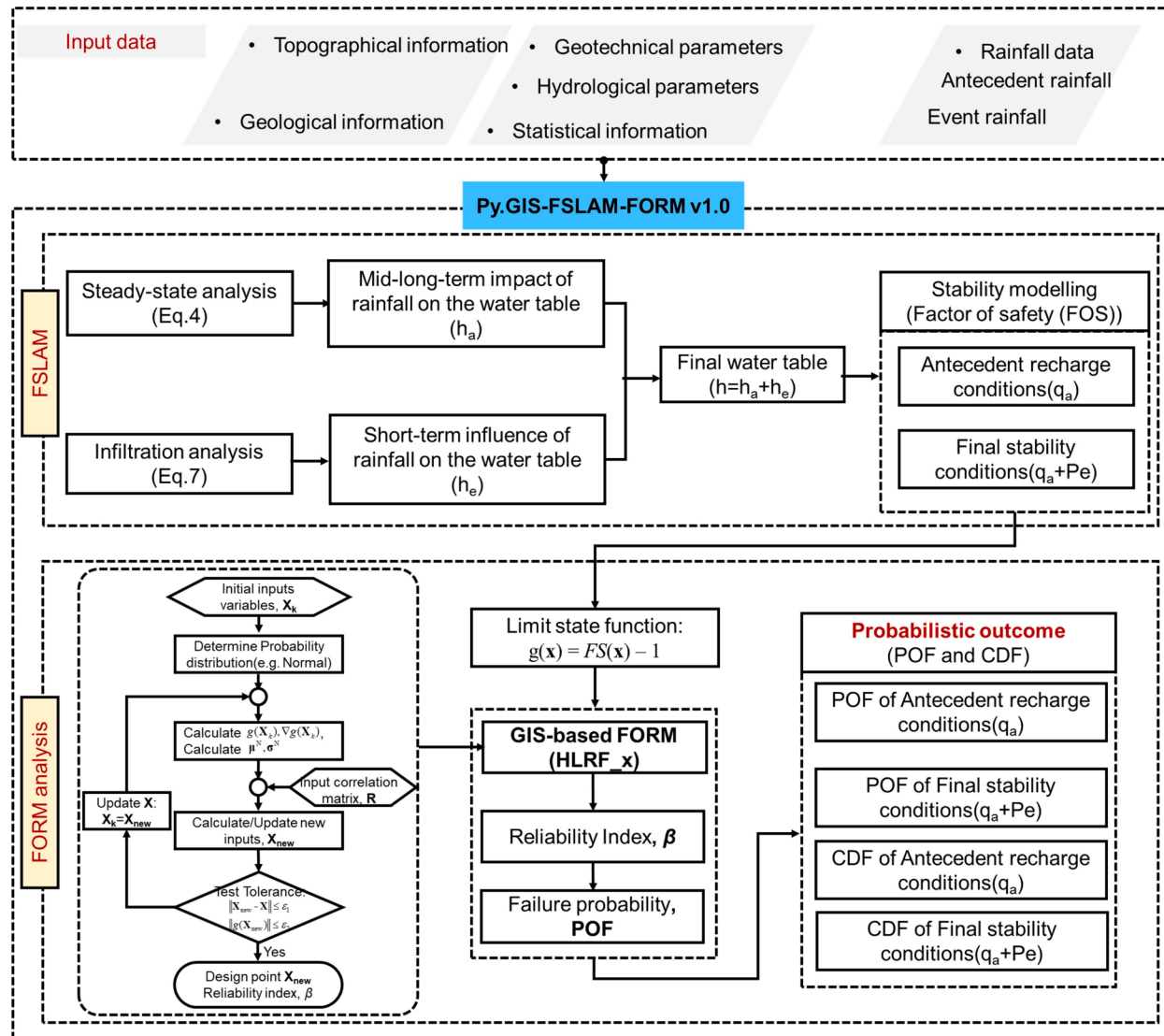


Fig. 2. The GIS-FSLAM-FORM computation workflow.

thresholds. The specific formulas are as follows:

$$FPR = \frac{FP}{FP + TN} \quad (13)$$

$$TPR = \frac{TP}{TP + FN} \quad (14)$$

where  $TP$  represents true positive predictions,  $TN$  represents true negative predictions,  $FP$  represents false positive predictions, and  $FN$  represents false negative predictions. This approach provides a balanced analysis of model accuracy and false positive rate, with higher AUC values indicating better predictive ability.

While the ROC curve is an important tool, other quantitative metrics such as the probability of detection (POD), balanced accuracy (BA), precision, recall or F1 score are also frequently used performance metrics to evaluate the method's accuracy. POD is calculated by comparing the number of true positive detections to the total number of actual targets, in our case observed landslides. The resulting value ranges from 0 to 1, with a higher value indicating a better performance of the model.

$$POD = \frac{TP}{(TP + FN)} \quad (15)$$

$$BA = \frac{TPR + TNR}{2} \quad (16)$$

$$ACC = \frac{TP + TN}{TP + TN + FP + FN} \quad (17)$$

$$Precision = \frac{TP}{TP + FP} \quad (18)$$

$$Recall = \frac{TP}{TP + FN} \quad (19)$$

$$F1\ score = \frac{2 \cdot Precision \cdot Recall}{Precision + Recall} \quad (20)$$

Furthermore, the distance to the perfect classification  $r$  proposed by Cepeda et al. (2010) is introduced to characterise the performance of the model as well:

$$r = \sqrt{(1 - TPR)^2 + FPR^2} \quad (21)$$

The  $r$ -value serves as an indicator of model performance. This metric quantifies the Euclidean distance between the TPR and FPR from perfect classification. A smaller value signifies a closer alignment of the model's

performance with perfect classification. In the case of best classification, the  $r$  assumes a value of 0 when TPR attains 1 and FPR reaches 0.

### 3. Data and landslide inventory

#### 3.1. Study area

The study area is located in the Central Pyrenees of Spain, covering 325.6 km<sup>2</sup>. Characterized by an Alpine Atlantic climate, it is influenced by Atlantic winds and the Pyrenees' orographic features. Val d'Aran, chosen for studying rainfall-induced landslides, experiences average temperatures between 5 and 9 °C and annual rainfall ranging from 900 to 1200 mm (Fig. 3 (a) and (b)). This high mountain region is notable for its history of slope failures, with a comprehensive catalogue of landslides providing data for model parameters. The region, with elevations from 700 to 3100 m asl, is geologically part of the Axial Pyrenees, featuring Paleozoic rock bedrock. Its landscape, shaped by various natural processes including glaciations and fluvial-torrential activities, presents a range of slopes where most landslides occur. The capital, Vielha, is situated at approximately 1000 m asl. There are eleven main lithological formations in the study area and their distributions are presented in Fig. 4a. The illustrate lithological class principally includes phyllite-slate (28.5 % of total area), mudstone (18.1 %), and colluvium (12.6 %), while conglomerate has minor significance (0.2 %) (Fig. 4b). The focus area boasts ten predominant land use and land cover categories (Fig. 4c), encompassing forest (43.1 % of the total area), grassland (30.8 %), and shrubs (16.7 %) (Fig. 4d).

#### 3.2. The 2013 landslide episode

On June 17th and 18th, 2013, the Val d'Aran region experienced multiple landslides and significant flooding due to heavy rainfall and snowmelt, causing economic losses of over 100 million euros. The Veilha meteorological station recorded 124.7 mm of rainfall in 48 h and 101.2 mm in 24 h. Meteorological reports indicated substantial snowmelt preceding and concurrent with the precipitation event. A comprehensive inventory consisting of 392 entries was meticulously compiled through the utilisation of aerial photographs, helicopter flights, and field surveys (Shu et al., 2019). In particular, small and shallow planar slides predominantly affect the uppermost soil layer within the study area of Val d'Aran region (Pyrenees, Spain). The infinite slope theory is highly applicable for analysing such types of failures (Hürlimann et al., 2022). Fig. 3(a) illustrates the landslide inventory map used to assess the spatial

distribution of landslides.

#### 3.3. Input dataset

The Py.FSLAM-FORM code integrates infinite modelling and hydrological modelling with the FORM probabilistic method. Consequently, the mandatory information includes geotechnical and hydromechanics parameters, along with their corresponding statistical relationships. The parameters utilized in this study were stored in the raster and text files as described in Section 2.3. The DEM was obtained from ICGC (2013), with a 5-m resolution. Additionally, the vector shapefile containing soil properties information was downloaded from ICGC (2016). The LULC information has been illustrated and reclassified in the above section which is down from CREAF (2020). The above-mentioned soil properties and LULC information are adapted from Hürlimann et al. (2022) as listed in Table 1 and Table 2. Furthermore, the extent of the area affected by snowmelt was determined by satellite images, while the quantity was estimated by snow-height measurements at weather stations. The final distribution of the effective water recharge into the terrain prior to the landslide episode (Fig. 5a) included two different values. The rate of water input was estimated at 0.5 mm/day for areas without snowmelt and 1.0 mm/day for areas where snowmelt was assumed to have added extra water to the soil (Fig. 5a). The data for  $P_e$  was estimated by combining the rainfall observed at different weather stations with the snowmelt that occurred during the landslide episode (Fig. 5b). The snowmelt related to  $P_e$  was approximated at 60 mm, which represents approximately 20 cm of snow assuming a snow density of 30%.

## 4. Results and discussion

Herein, insights into the results of landslide susceptibility assessment are provided, which were predicted using a physically-based probabilistic modelling based on FSLAM-FORM. According to studies conducted in Val d'Aran, this analysis highlights the importance of considering parameters' COV, correlation, and distribution types under two hydrological conditions: antecedent recharge and its combination with event rainfall.

#### 4.1. Probabilistic analysis

Herein, the susceptibility of rainfall-induced shallow landslides under two typical hydrological conditions and the uncertainties of

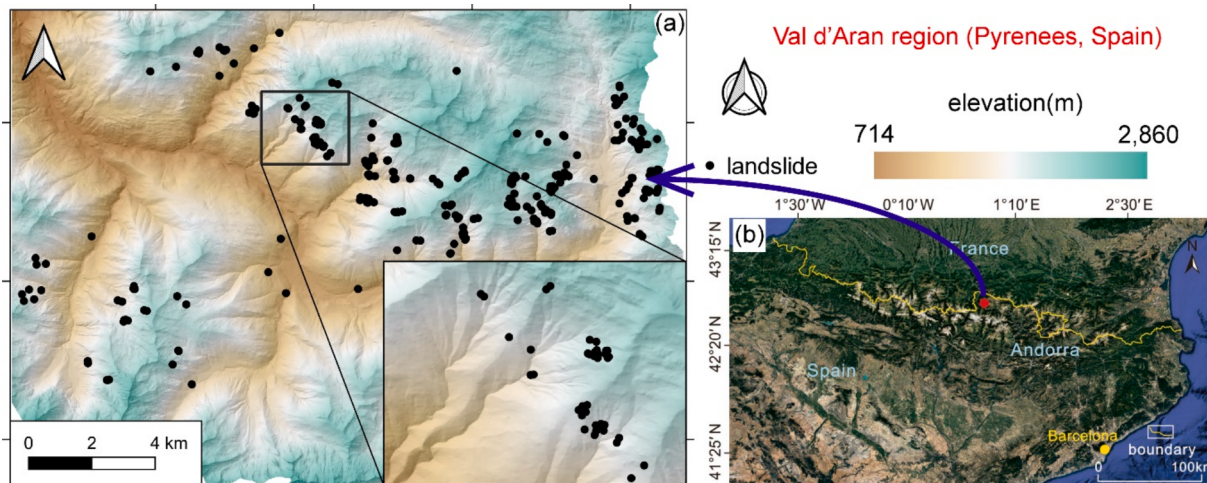


**Fig. 3.** Val d'Aran region (a) digital elevation model including the landslides observed during the 2013 episode (adapted from Hürlimann et al. (2022)), (b) location of the study area in the Pyrenees (red dot), the effect of elevation. (For interpretation of the references to colour in this figure legend, the reader is referred to the web version of this article.)

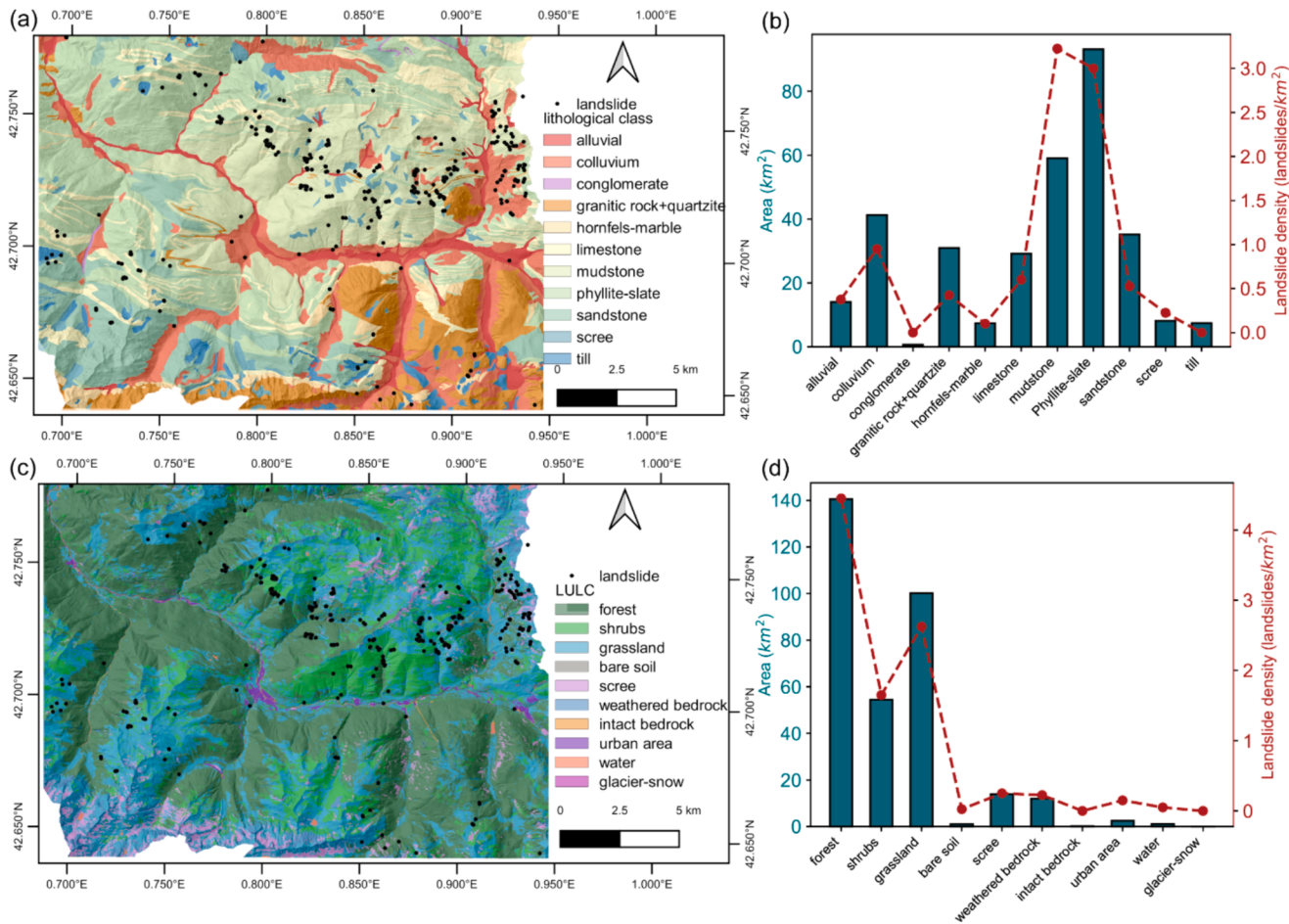


**Fig. 4.** The input raster maps of the Val d'Aran region: (a) a reclassified lithological map that provided the soil properties, (b) the influence of each class on the slope failure, (c) a reclassified land use and land cover map, (d) the influence of each class on the slope failure.

geotechnical parameters are investigated. The 'density heat and contour' analysis (Yuan et al., 2019) was performed to illustrate the spatial distribution of either observed landslide occurrences or predicted susceptibility zones. This distribution is depicted across various slope gradients and aspects, utilising contour lines for visual representation.

The regions with very high susceptibility ( $POF > 0.9$ ) under distinct hydrological scenarios are illustrated in Fig. 6a. These scenarios include antecedent recharge ( $q_a$ ) and the combination of effective antecedent recharge and event rainfall ( $q_a + P_e$ ). Conversely, Fig. 6b also illustrates the density distribution of landslide occurrences obtained through field surveys by employing 'density heat and contour' maps. The intensity and depth of the colours in the contours are directly proportional to the frequency of landslides. Darker and denser contours indicate areas characterized by elevated landslide probabilities, influenced by specific slope gradients, aspects, and hydrological conditions. These contours effectively delineate zones exhibiting the highest concentration of landslides. Therefore, the density heat maps reveal a significant clustering of landslides in areas with certain slope grades and aspects. This is particularly evident in regions with slope inclinations between 30 and 40 degrees as an aspect between 100 degrees and 250 degrees. The contour distribution corroborates this observation, aligning closely with the actual landslide locations documented in field surveys.

Fig. 6c compares the density distribution of regions with very high susceptibility under antecedent recharge ( $q_a$ ) and combined antecedent recharge and event rainfall ( $q_a + P_e$ ) conditions. The results demonstrate a significant increase in the area classified as having very high failure rates under event rainfall conditions ( $q_a + P_e$ ), indicating an elevated probability of landslides. The heightened susceptibility of landslides is

particularly evident on slopes that are already saturated due to effective antecedent recharge, as the addition of rainfall significantly exacerbates this phenomenon. A comparison between scenarios solely involving  $q_a$  (indicated by a green star) and those combining  $q_a$  and  $P_e$  shows that the latter scenario exhibits a notably higher density and distribution of landslides. The discussed points highlight the critical role of the interaction between hydrological conditions in determining landslide susceptibility. This implies that the increased risk due to event rainfall accentuates its contribution to slope instability. The strong spatial correlation between the POF and the synergistic effect of antecedent recharge and event rainfall in highly susceptible regions confirms the crucial influence of event rainfall on landslides, especially in areas pre-saturated with effective antecedent recharge. Moreover, the congruence between the areas of very high susceptibility and the locations of actual landslides validates the model's ability to accurately identify regions with elevated landslide susceptibility. This illustrates the effectiveness of probabilistic methods in evaluating landslide susceptibility as well.

In summary, landslide occurrences are influenced by various inter-related factors such as hydrological conditions, geological attributes, and geomorphological features. This study specifically addresses hydrological triggers, primarily focusing on effective antecedent recharge and its combined impact with event rainfall ( $q_a + P_e$ ). Effective antecedent recharge describes the moisture content in the soil before a rainfall event, influenced by factors like surface runoff and plant transpiration. These elements decrease the soil's ability to absorb more rain, leading to moisture accumulation that weakens the soil's mechanical integrity, particularly its shear strength. This weakening heightens slope vulnerability to destabilisation from additional rain or external forces.

**Table 1**

Best-fit values of the soil properties obtained during the calibration phase. The properties are separated regarding the different lithological classes. HSG stands for hydrologic soil group (USDA, 2007) (Adapted from Hürlimann et al. (2022)).

Lithological class	$C_s$ -min/ max (kPa)	$\varphi$ -min/ max(°)	z (m)	K(m/ s)	n (–)	$\rho_s$ (kg/ m³)	HSG (–)
Alluvial	0/3	35/45	4	$1 \times 10^{-3}$	0.3	2000	A
Colluvium	1/3	25/35	1.5	$1 \times 10^{-6}$	0.3	2000	B
Scree	0/3	40/50	3	$1 \times 10^{-2}$	0.4	2000	A
Till	0/5	30/40	2	$1 \times 10^{-5}$	0.3	2000	B
Conglomerate*	0/5	35/45	3	$1 \times 10^{-5}$	0.35	2000	A
Sandstone*	1/5	35/45	3	$1 \times 10^{-4}$	0.35	2000	A
Mudstone*	1/5	20/30	2	$1 \times 10^{-6}$	0.3	2000	B
Granitic rock + quartzite*	0/4	35/45	2	$1 \times 10^{-5}$	0.3	2000	A
Hornfels- marble*	1/3	30/40	2	$1 \times 10^{-5}$	0.3	2000	A
Limestone*	1/3	20/35	1.5	$1 \times 10^{-6}$	0.3	2000	B
Phyllite-slate*	0/5	20/35	2	$1 \times 10^{-6}$	0.3	2000	B

HSG: Hydrological-Mechanical Terrain Units and land use are associated with a CN value, which is provided by USDA (2007).

\* The soil properties refer to the soil layer covering this bedrock type.

**Table 2**

Best-fit values of the root cohesion ( $C_r$ ), and the curve number (CN), obtained during the calibration phase. The values are separated regarding the different LULC classes (adapted from Hürlimann et al. (2022)).

LULC	$C_r$ -min/max (kPa)	CN-A (–)	CN-B (–)	CN-C (–)	CN-D (–)
Forest	4/14	40	60	69	76
Shrubs	3/6	43	65	76	82
Grassland	2/4	49	69	79	84
Bare soil	0/0	77	86	91	94
Scree	0/0	30	30	30	30
Weathered bedrock	0/0	77	86	91	94
Intact bedrock	0/0	77	86	91	94
Urban area	0/1	90	92	96	98
Water	999/999	100	100	100	100
Glacier-snow	999/999	100	100	100	100

Note: 999 means invalid value.

During rainfall, increased soil moisture quickly raises pore water pressure and diminishes effective stress which accelerates the onset of slope failures. This research highlights the crucial importance of comprehending the combined effects of  $q_a$  and  $P_e$  in precipitating rainfall-induced landslides.

#### 4.2. Effect of COVs on the spatial distribution of predicted landslides using GIS-FLAM-FORM under different hydrological conditions

##### 4.2.1. Impact of COV on the spatial distribution of probabilistic landslide susceptibility

The precision of failure probability predictions in landslide susceptibility analysis hinges on accurately determining the uncertainties of input data parameters. One significant factor influencing this accuracy is the COV. In our study, under the assumption that all parameters follow the normal distribution, we analysed the impact of various COVs on landslide susceptibility outcomes, specifically COV = 0.01, 0.1, 0.3, 0.5.

The relevant soil and vegetation property values are detailed in Table 3 and Table 4.

Landslide susceptibility analyses were conducted using the FSLAM-FORM by varying different COVs for input parameters. Table 5 presents the statistical results of the landslide susceptibility frequency ratio under different hydrologic conditions ( $q_a$  and  $q_a + P_e$ ). Specifically, Under the condition of antecedent recharge and a COV of 0, most landslides (72.12 %) happened in Class V areas (very high susceptibility), with no occurrences in Class I to IV areas (varying from very low to high susceptibility). With the COV rising to 0.1, landslides in Class V areas dropped slightly to 58.57 %, with a new emergence of landslides in Class IV areas (13.55 %). As the COV further increased to 0.3 and 0.5, the frequency of landslides in Class V areas continued to decrease, whereas Class III and IV areas saw an increase, suggesting that the model's precision in identifying very high-susceptibility areas lessened with higher COVs, and its sensitivity towards detecting high-vulnerability areas increased.

In addition, for the condition of  $q_a + P_e$ , 74.7 % of the landslides were in areas of very high susceptibility, whereas 25.3 % were in zones of very low susceptibility when ignoring parameter variability. As a result, the frequency ratio of landslides escalated notably from zones of low to very high susceptibility, increasing from 0.36 to 2.6. This suggests that the FSLAM-FORM model is effective in detecting most historical landslides when actual rainfall data is incorporated.

In contrast, as COV increased from 0.1 to 0.5, the percentage of actual landslides in areas with very low susceptibility decreased rapidly (from 63.2 % to 14.3 %), and the areas classified as having very high susceptibility decreased significantly (from 10 % to 0). Additionally, the ratio of landslide frequency in high and very high susceptibility areas (IV and V) increased from 3.4 to 5, especially in moderately sensitive regions. These findings suggest that model identification of high-susceptibility areas is highly sensitive to variations in COV. The next step in this section is to explore in detail the proportional changes in the spatial distribution of failure probabilities at different COVs.

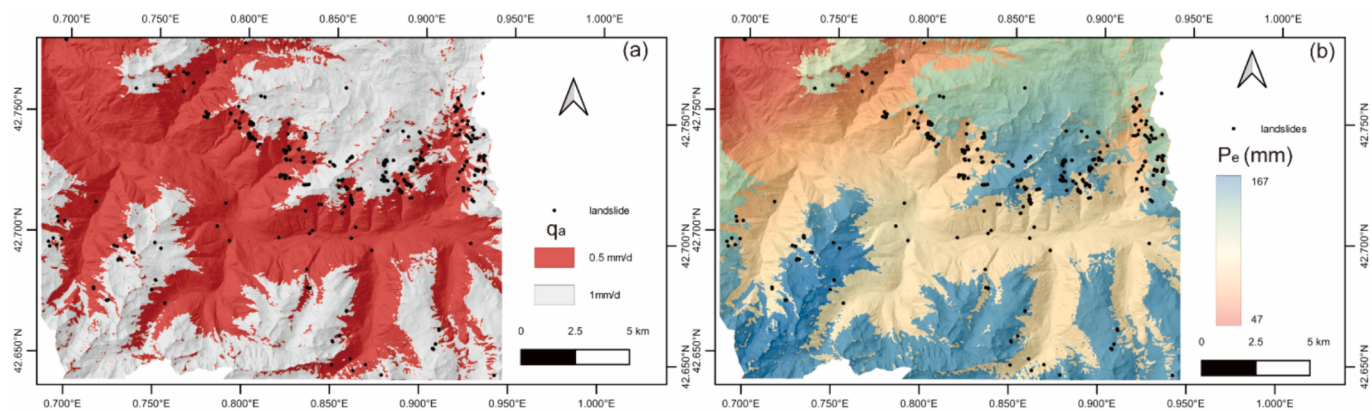
To ensure the representativeness of feature samples across the entire area and comprehensively evaluate the model's performance, a comparative analysis was conducted. This involved comparing 392 source points from the landslide inventory with 5000 randomly selected points obtained through systematic random sampling (Medina et al., 2021). Additionally, it is important to note that both datasets were normalized based on point count and subsequently presented as percentages relative to the POF.

Fig. 7 depicts the distribution interval of POF, indicating that significant changes in the failure probability of landslide sites occur primarily within intervals above high sensitivity, while changes in non-landslide sites are predominantly observed within low sensitivity intervals. With increasing COV, the variation of non-slip points near low failure probabilities becomes more pronounced. For example, in the  $q_a + P_e$  scenario, non-landslide points within the very low failure probability range (0–0.01) drop sharply from 71.6 % to 11.9 %, while landslide points in the very high failure probability range (0.9–1.0) decrease significantly from 74.7 % to 7.9 %. These results demonstrate that the FSLAM-FORM method proficiently reflects the influence of rainfall on landslide susceptibility and accurately simulates the impacts on both landslide and non-landslide points considering parameter variability on the regional scale.

##### 4.2.2. Impact of COVs on failure probability considering hydrological conditions

To further investigate the disparities in the impact of parameter variability on landslide susceptibility, we also analysed the proportion of raster showing very high susceptibility (POF > 0.9) regions under different hydrological conditions.

Fig. 8 illustrates how incorporating uncertainty in geotechnical parameters, particularly COV affects the assessment of susceptibility to rainfall-induced shallow landslides across various hydrological



**Fig. 5.** Rainfall and snowmelt conditions of the 2013 landslide episode used for the model calibration. (a) Antecedent water recharge,  $q_a$ , and (b) event water recharge,  $P_e$ . Both maps include the locations of the landslides that were used during the calibration phase (adapted from Hürlimann et al. (2022)).

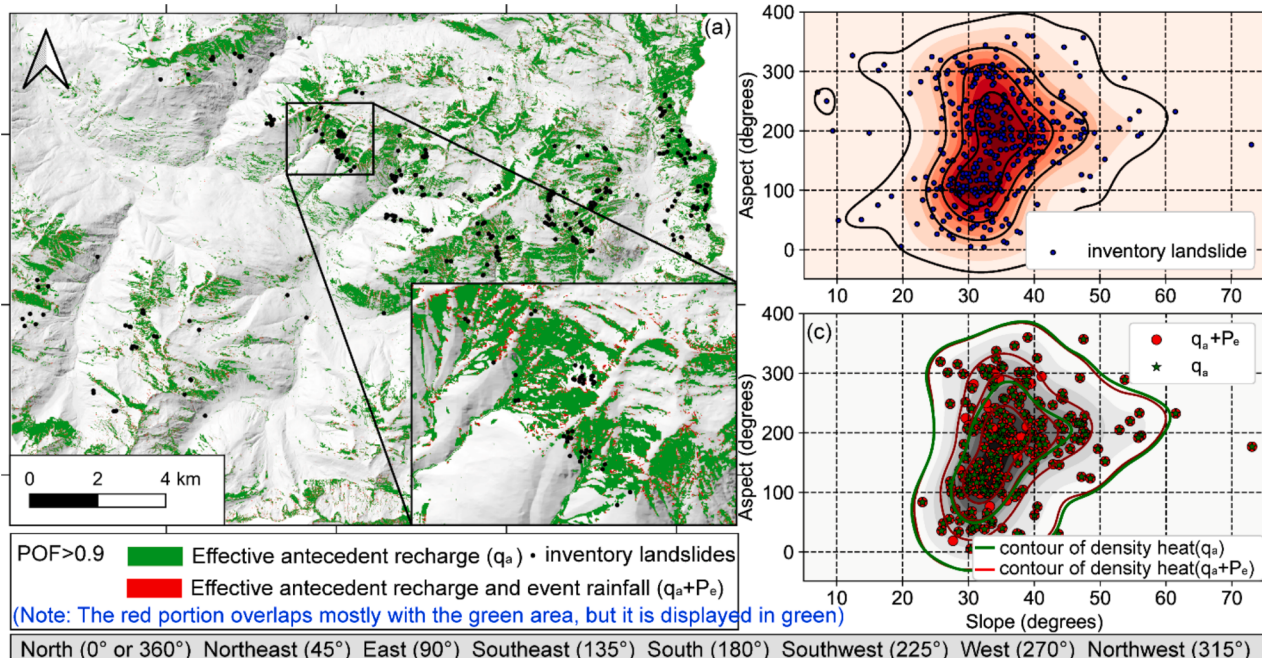


**Fig. 6.** (a) Distribution maps of areas with very high susceptibility (POF > 0.9) under conditions of effective antecedent recharge ( $q_a$ ) and combined effective antecedent recharge and event rainfall ( $q_a + P_e$ ). Kernel density estimation of: (b) all the inventory points by slope and aspect, (c) areas of very high susceptibility under  $q_a$  and  $q_a + P_e$  conditions, segmented by slope and aspect.

**Table 3**

The values of soil properties (cohesion,  $C_s$ , and friction angle,  $\phi$ ) account for different COVs.

Soil parameters		$C_s$ -mean(kPa) ( $\mu$ )	$\phi$ -mean( $^{\circ}$ ) ( $\mu$ )	Distribution	COV	Standard deviation ( $\sigma$ )
Lithological class	Alluvial	1.5	40	Normal	0.01,	$\sigma = \mu \bullet \text{COV}$
	Colluvium	2	30		0.10,	
	Scree	1.5	45		0.20,	
	Till	2.5	35		0.30,	
	Conglomerate*	2.5	40		0.40,	
	Sandstone*	3	40		0.50	
	Mudstone*	3	25			
	Granitic rock + quartzite*	2	40			
	Hornfels-marble*	2	35			
	Limestone*	2	27.5			
	Phyllite-slate*	2.5	27.5			

\* The soil properties refer to the soil layer covering this bedrock type.

**Table 4**The values of the root cohesion ( $C_r$ ) account for different COVs.

LULC parameters	$C_r$ -mean (kPa) ( $\mu$ )	Distribution	COV	Standard deviation ( $\sigma$ )
Forest	9	Normal	0.01,	$\sigma = \mu \cdot \text{COV}$
Shrubs	4.5		0.10,	
Grassland	3		0.20,	
Bare soil	0		0.30,	
Scree	0		0.40,	
Weathered bedrock	0		0.50	
Intact bedrock	0			
Urban area	0.5	—	—	—
Water	999			
Glacier-snow	999			

Note: 999 means an invalid value.

scenarios. In particular, Fig. 8a and b display the spatial distribution of areas with very high susceptibility (POF > 0.9) considering only effective antecedent recharge ( $q_a$ ) and in combination with event rainfall ( $q_a + P_e$ ), respectively. The varied colours in these figures represent the differences in outcomes when different COVs are included versus when COV is not considered. The analysis indicates that areas classified as highly susceptible become more spatially distinct with increasing COV. This implies that increasing uncertainty in geotechnical parameters does not necessarily expand the very high susceptibility areas. Instead, it leads to a more dispersed distribution of regions with moderate to high susceptibility. Importantly, model predictions show greater distinction in scenarios including event rainfall ( $P_e$ ), underscoring the idea that event rainfall intensifies the uncertainty in landslide susceptibility.

Fig. 8(c-f) display the distribution of actual landslide locations and

areas of very high susceptibility (using random points) for different values of the COV through density heat and slope-direction contour plots. As shown in Fig. 8(c-f), the distribution of landslide points becomes more scattered as COV increases which indicates that increased uncertainty in geotechnical parameters can lead to greater unpredictability in locating landslides. Higher concentrations of landslides are noted in areas with slopes of 30–40 degrees and slope aspects of 150–200 degrees. In Fig. 8(g-j), the distribution of random points is more discrete than the actual landslide locations at high COV values which highlights the significant influence of parameter variability.

Adding event rainfall ( $P_e$ ) results in a more distinct distribution of landslide predictions, even when the COV is held constant. This is observed when comparing landslide susceptibility solely under effective antecedent recharge ( $q_a$ ) with the combined influence of  $q_a$  and event rainfall ( $q_a + P_e$ ). This phenomenon is caused by rainfall changing the water table, which impacts the soil's stress-strain characteristics and ultimately its stability. Meanwhile, with event rainfall ( $P_e$ ), the area classified as highly susceptible expands, underscoring the combined impact of hydrological conditions and geotechnical parameter uncertainty on potential landslide scenarios. However, a detailed analysis will be performed to understand how antecedent recharge and event rainfall influence the probabilistic spatial distribution of landslides, particularly considering changes in the COV.

Additionally, the relationship between the COV of the parameter and the proportion of highly sensitive regions is evident, as previously demonstrated. To comprehensively capture the system behaviour under investigation across a spectrum of rainfall events, in our graph, we represented the x-axis using ranges of event rainfall instead of specific values, which helps mitigate outlier effects and provides a clearer understanding of dataset central tendency and dispersion. This approach facilitates trend identification and inference-making regarding data

**Table 5**

The frequency ratio considers COVs under different hydrological conditions for various susceptibility levels.

Hydrological conditions	Susceptibility levels	Percentage of landslide numbers (%)				Percentage of graded area (%)				Frequency ratio			
		COV	0	0.1	0.3	0.5	0	0.1	0.3	0.5	0	0.1	0.3
$q_a$	I	27.88	12.02	1.53	0.00	72.97	54.39	16.67	2.23	0.38	0.22	0.09	0.00
	II	0.00	6.39	3.84	2.05	0.00	9.16	23.40	18.81	0.00	0.70	0.16	0.11
	III	0.00	9.46	22.51	25.83	0.00	9.41	32.89	51.92	0.00	1.01	0.68	0.50
	IV	0.00	13.55	40.66	58.31	0.00	7.67	17.78	23.13	0.00	1.77	2.29	2.52
	V	72.12	58.57	31.46	13.81	27.03	19.36	9.25	3.90	2.67	3.02	3.40	3.54
$q_a + P_e$	I	25.32	9.97	1.53	0.00	70.74	51.41	15.79	2.28	0.36	0.19	0.10	0.00
	II	0.00	5.37	3.58	1.79	0.00	9.38	21.61	17.57	0.00	0.57	0.17	0.10
	III	0.00	9.97	20.20	23.53	0.00	9.95	33.34	50.89	0.00	1.00	0.61	0.46
	IV	0.00	11.51	39.90	60.36	0.00	8.08	18.86	24.74	0.00	1.42	2.12	2.44
	V	74.68	63.17	34.78	14.32	29.26	21.18	10.40	4.52	2.55	2.98	3.34	3.17

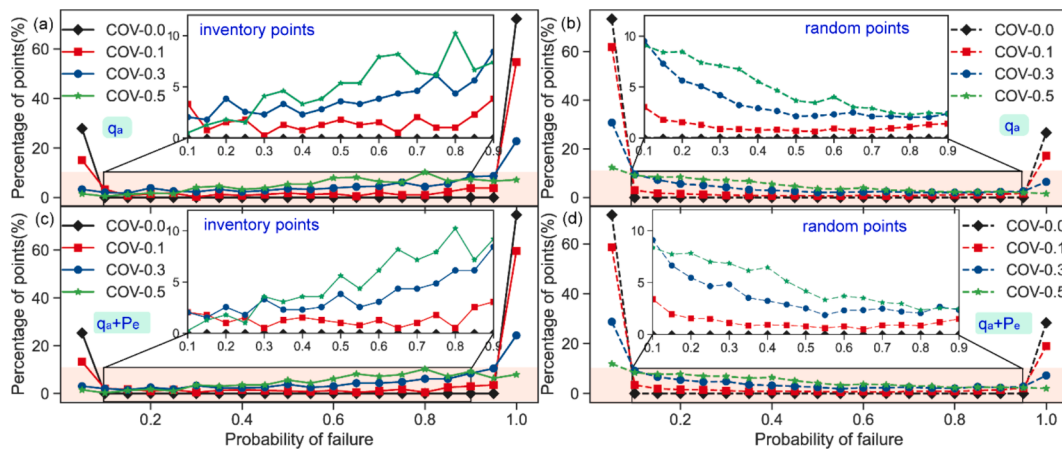
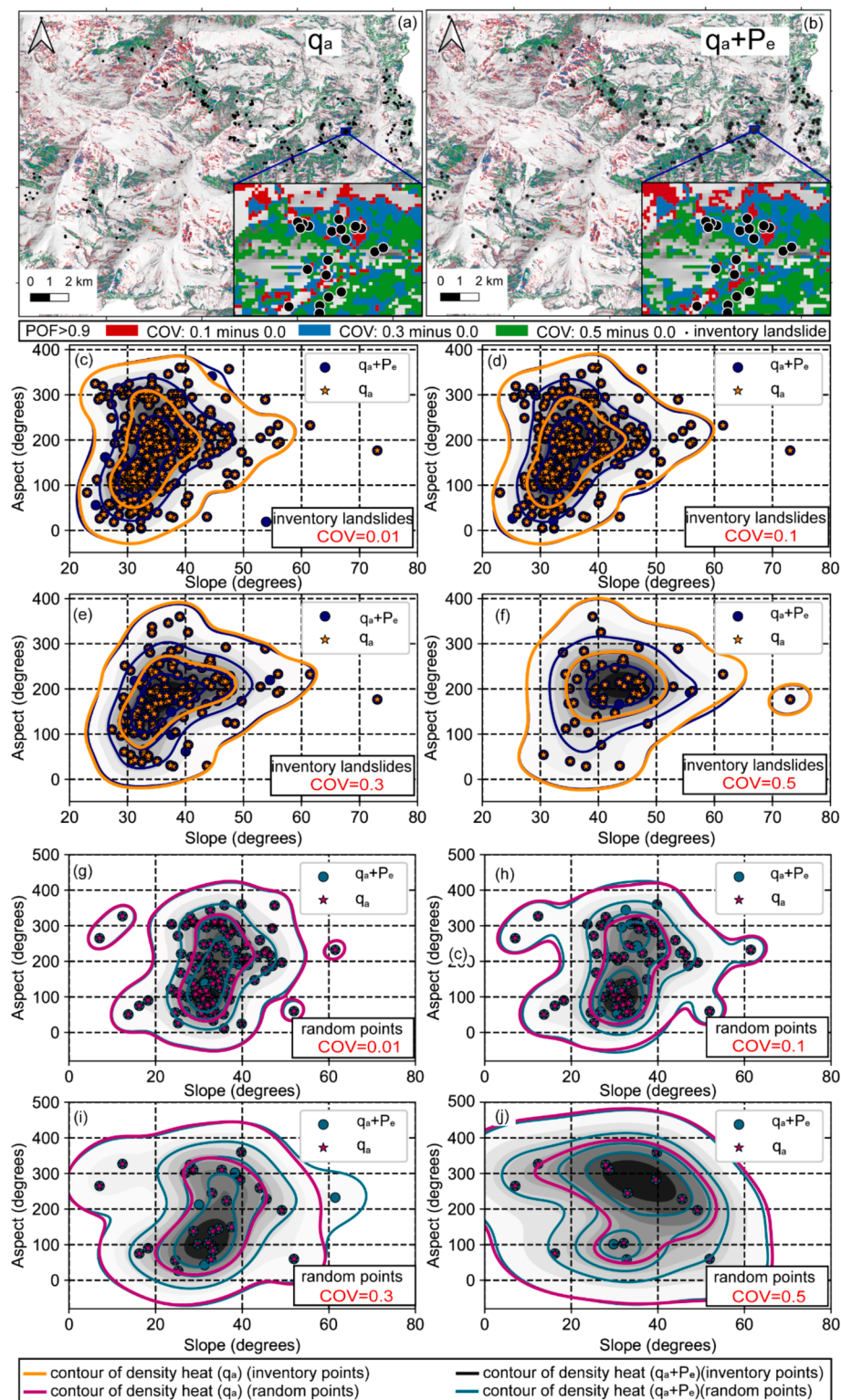


Fig. 7. Comparison between inventory points and random points under different rainfall conditions and COVs: only antecedent rainfall for (a) inventory points; (b) random points; antecedent and event rainfall for (c) inventory points; (d) random points.



**Fig. 8.** (a) Impact of COV variations on the areas with very high susceptibility ( $POF > 0.9$  under different hydrological conditions( $q_a$ ) and ( $q_a + P_e$ )). Kernel density estimation of areas of very high susceptibility under  $q_a$  and  $q_a + P_e$  conditions, segmented by slope and aspect: (c–f); random points (g–j).

distribution within these intervals. As shown in Fig. 9, under a 0.5 mm/d antecedent recharge condition, there is a significant variation in the proportion of very high susceptibility areas for event rainfalls ranging from 77 to 107 mm, regardless of the COV. Specifically, as the COV increases by 0.5 from zero, the corresponding proportion decreases from 12.6 % to 2 %. On the other hand, the region affected by a preceding rainfall of 0.1 mm/d and event rainfall ranging from 137 to 167 mm

undergoes the most substantial change in heightened sensitivity, with a decrease from 11.8 % to only 1.5 %. This suggests that an increase in event rainfall does not lead to a proportional increase in the likelihood of failure under amplified antecedent rainfall conditions.

Fig. 9 depicts the change of relative percentage for  $POF > 0.9$  areas across varying  $P_e$  intervals under two distinct antecedent rainfall conditions ( $q_a = 0.5$  mm/d,  $q_a = 1.0$  mm/d). Specifically, there is a

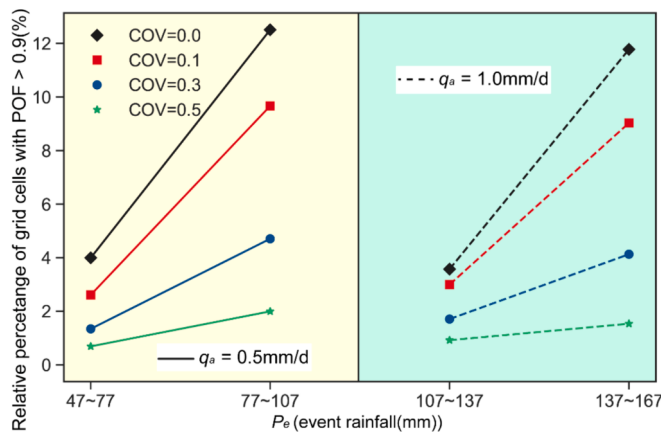


**Fig. 9.** Effect of the two rainfall inputs (antecedent ( $q_a$ ) and event rainfall ( $P_e$ )) on the percentage of very high susceptibility areas (POF  $> 0.9$ ) with the variation of COVs.

corresponding increase in the relative proportion in the very high probability region as the event rainfall increases under the antecedent rainfall recharge of  $q_a = 0.5 \text{ mm/d}$  and  $q_a = 1.0 \text{ mm/d}$ . The area under  $q_a = 0.5 \text{ mm/d}$  with POF  $> 0.9$  slightly exceeds that under  $q_a = 1.0 \text{ mm/d}$  in the 107–137 mm and 137–167 mm intervals in the event rainfall range of 47–77 mm and 77–107 mm. Based on the aforementioned analysis, it is evident that there has been an increase in the proportion of regions with medium and high susceptibility while the proportion of regions with a very high POF has decreased. This phenomenon can primarily be attributed to the impact of varying rainfall conditions on groundwater seepage (Medina et al., 2021). In other words, as precipitation values increase, the rate at which grid failure probability increases slows down due to saturation on the slope. As a result, the impact of rainfall infiltration on failure probability becomes less significant compared to situations involving smaller event rainfall. Event rainfall induces vertical groundwater flow and affects the damage probability of the grid at the infiltration point. On the other hand, antecedent recharge leads to lateral groundwater flow, which may impact the groundwater level at other points surrounding the grid, thereby increasing its failure probability. In conclusion, the increase in lateral groundwater flow (i.e., the consequence of an increase in  $q_a$ ) can result in a reduction of the overall extent of extreme susceptibility regions (very low and very high), whereas an expansion of high susceptibility regions occurs in contrast.

It is additionally observed that Fig. 9 illustrates an increase in the COV value leads to a decrease in the proportion of extremely high susceptibility areas. This is attributed to the reclassification of areas initially categorized as very low or low susceptibility into medium or high susceptibility, while areas originally classified as extremely high susceptibility have also undergone a similar reclassification. These findings demonstrate that the uncertainty of parameters can significantly impact the spatial distribution of extremely high susceptibility areas, aligning with the analysis presented in the preceding section.

#### 4.2.3. Combined comparison of spatial distribution probabilities for landslide impacts considering variations in COVs and hydrological conditions

Regarding the effects of variations in input parameters, our main focus is on the impact of statistical information on landslide susceptibility assessment. This includes exploring different COVs of  $c$  and  $\phi$ , their cross-correlation coefficients, as well as the influence of non-normal distribution. First, in geotechnical engineering, the shear strength parameters of soils, such as cohesion and friction angle, play a crucial role in assessing slope stability. These parameters are subject to a certain level of randomness, which can arise from environmental factors and changes in the physical properties of the materials themselves. The

true values of shear strength parameters fluctuate within a certain range due to the inherent uncertainty, leading to challenges and risks in landslide prediction. In other words, this kind of uncertainty can directly affect the accuracy of the assessment results. Therefore, a suitable index is needed to measure this uncertainty. As described in Section 4.2, the COV is calculated by dividing the standard deviation by the mean. This is the standardised statistical indicator that can characterize the relative fluctuation degree of a random variable. In this study, the FSLAM primarily considers the variability of shear strength parameters for both soil and vegetation, namely cohesion and friction angle. When solely considering shear strength parameters for the same limit state function, an increase in COV leads to higher uncertainty. This leads to greater dispersion of data and higher POF. This means that larger shear strength variations may contribute to slope instability or even induce landslides. This is mainly because the change in COV affects the shape of the joint probability density function (PDF). An increase in COV causes the corresponding joint PDF curve to become broader and lower, resulting in a significant rise in POF. These findings align with the studies conducted by Tang et al. (2013) and Ma et al. (2022). When COV is smaller, the variation range of the stochastic parameters is correspondingly narrower, thus the distribution of the PDF is tighter as well. As a result, the associated failure probability is lower. Therefore, the variability of the geotechnical materials should be considered in the regional landslide sensitivity analysis.

In addition, the increase of the COV alone does not significantly increase the probability of damage, but primarily increases the absolute value of damage probability for individual grid cells, with limited impact on areas with initially very low or low hazard levels. Conversely, increasing the COV substantially increases the overall landslide hazard in the area, mainly by causing many regions originally classified as very low or low-hazard to transition into medium or even high-hazard zones. The proportion of highly hazardous areas decreases, and there is a shift towards an inclination for high-hazard regions. This again highlights the importance of considering parameter variability when assessing landslide susceptibility under rainfall conditions using the physical model at a regional scale.

In conclusion, the variability of geotechnical parameters, particularly cohesion and internal friction angle, plays a pivotal role in assessing the susceptibility of rainfall-induced shallow landslides. An increase in COV significantly impacts the stability of model predictions, leading to heightened spatial uncertainty in landslide forecasts. This effect is particularly pronounced when considering event rainfall, emphasizing the vital role of changing hydrological conditions in landslide occurrences. Therefore, integrating uncertainties in both geotechnical parameters and hydrological conditions into models is essential for accurately predicting landslide susceptibility assessment.

#### 4.3. Effect of statistical correlation and non-normal distribution on the spatial distribution of predicted landslides using GIS-FLAM-FORM

##### 4.3.1. Impact of statistical correlation and non-normal on the spatial distribution of probabilistic landslide susceptibility

Considering the correlation between various physical parameters plays a critical role in regional probabilistic landslide analysis. Correlation quantifies the relationships between random variables, such as terrain height, rainfall, and soil type, which can affect the likelihood of landslides. It is essential to model correlations and non-normal distributions to enhance the rationality and accuracy of landslide susceptibility assessments. In this study, to focus on the negative correlation between cohesion ( $c$ ) and friction angle ( $\phi$ ), the lognormal distribution was used, while keeping the remaining three parameters (soil depth ( $z$ ), saturated hydraulic conductivity ( $K$ ), soil porosity ( $n$ ), and density of saturated soils ( $\rho_s$ )) as constant. Table 4 lists the default mean values for the parameters, with a COV of 0.1. The correlation coefficient of 0.5 was used to analyse the impact of correlation on landslide probability, as suggested by Tang et al. (2013).

The FSLAM-FORM method was used to calculate landslide susceptibility. Fig. 10a shows the results of the susceptibility analysis for parameters following a correlated lognormal distribution, considering effective antecedent recharge and event rainfall. The observed landslides were mainly concentrated in areas classified as areas with very high susceptibility (POF > 0.9). Fig. 10b presents the percentage of landslide susceptibility for each of the five levels: very low, low, moderate, high, and very high. These categories accounted for 10.1 %, 10.1 %, 16.2 %, 10.4 %, 44.4 %, and 18.9 % of the overall samples, respectively. Note that these results were summarised based on four statistical distributions of the parameters, grouping all outcomes belonging to the same category. For example, the “very low” section (I) of the pie chart includes all results falling within the very low susceptibility range, regardless of whether they were normal uncorrelated, normal correlated, lognormal uncorrelated, or lognormal correlated data. Notably, the parameters subjected to lognormal correlation contributed to 27 % of the region associated with very high sensitivity, indicating the significant influence of non-normal and interrelated parameters on the prediction of potential landslides.

To further investigate the effect on landslide susceptibility of varying the cross-correlation between  $c$  and  $\varphi$  under different hydrological conditions, a comparison of the proportions of failure probability was listed in Table 6. Overall, as the cross-correlation coefficient changes from 0 to  $-0.7$ , the very higher susceptibility region ( $POF \geq 0.9$ ) observed an increasing trend.

Specifically, the analysis solely focusing on the impact of antecedent recharge reveals that 16.1 % of landslides occur in areas exhibiting high susceptibility to landslides when disregarding parameter correlations, while 43.9 % of total regions with low susceptibility. The change in landslide frequency from low susceptibility to very high susceptibility is not statistically significant which values increasing marginally from 0.16 to 0.22. However, it is noteworthy that a substantial proportion of observed landslides (58.1 %) occurred in areas classified as highly susceptible, while only a small percentage (6.6 %) were recorded in areas categorised as highly non-susceptible when considering  $q_a + P_e$  condition. The frequency of landslides significantly increases from 0.16 to 3.31 as we move from areas with low susceptibility to those with very high susceptibility, indicating that FSLAM-FORM has the potential to effectively identify most historical landslides when considering different hydrological scenarios. In addition, as the negative correlation coefficient increases from 0.1 to 0.7, there is no significant increase in the actual percentage of landslides in the very low susceptibility area (from 6.6 % to 9.2 %) compared with the proportion of areas classified as very

high susceptibility slowly increases (from 58.1 % to 64.7 %). Furthermore, both high and very-high susceptibility areas (IV and V) exhibit a gradual decrease in landslide frequency.

#### 4.3.2. Impact of statistical correlation and non-normal on failure probability considering hydrological conditions

To further investigate the impact of parameter cross-negative correlations and different statistical distributions on landslide hazards across various rainfall ranges, we examined the proportion of extremely high-susceptibility areas ( $POF > 0.9$ ). Fig. 11 presents the impact of negative correlation (indicated by the correlation coefficient  $\rho$ ) of geotechnical parameters on the prediction of rainfall-induced shallow landslide susceptibility under varied hydrological scenarios. Fig. 11a–b illustrate the spatial distribution of landslide susceptibility considering solely effective antecedent recharge ( $q_a$ ) and the combination of  $q_a$  with event rainfall ( $q_a + P_e$ ), respectively. The analysis reveals that a decrease in  $\rho$  (i.e., an increase in negative correlation) leads to a more spatially distinct very high susceptibility region ( $POF > 0.9$ ). This distinctness is more evident when event rainfall ( $q_a + P_e$ ) is included. This also suggests a heightened impact of rainfall events on landslide distribution predictions in the context of a strong negative correlation among geotechnical parameters. Fig. 11(c–l) highlight the variance in the distribution of actual versus random landslide points across different levels of negative correlation. These results show the spatial density of heat against slope and aspect. At  $\rho = 0$  (Fig. 11c–g), the landslide distribution predictions are relatively centralized. However, as  $\rho$  decreases to  $-0.7$ , the contour distribution of landslide point probability density becomes more dispersed. This indicates a stronger negative correlation between the angle of internal friction and cohesion increases prediction uncertainty in landslide susceptibility. Additionally, Fig. 11(h–l) depict the transformation of very high sensitivity regions from discrete to concentrated as  $\rho$  shifts from 0 to  $-0.7$ . This change reflects an enhanced sensitivity of the model to landslide susceptibility predictions due to increased negative correlation.

Regarding the effects of  $q_a$  and  $q_a + P_e$  conditions, the density contours of landslide predictions are notably discrete under  $q_a$ -only scenarios. This implies that negative correlations among geotechnical parameters may exert a lesser impact on landslide susceptibility under antecedent recharge condition.

Conversely, the probability density contours become more widespread for all values of  $\rho$  when experiencing the  $q_a + P_e$  condition. This indicates that event rainfall intensifies the negative correlation effect between cohesion and the internal friction angle, thereby raising the

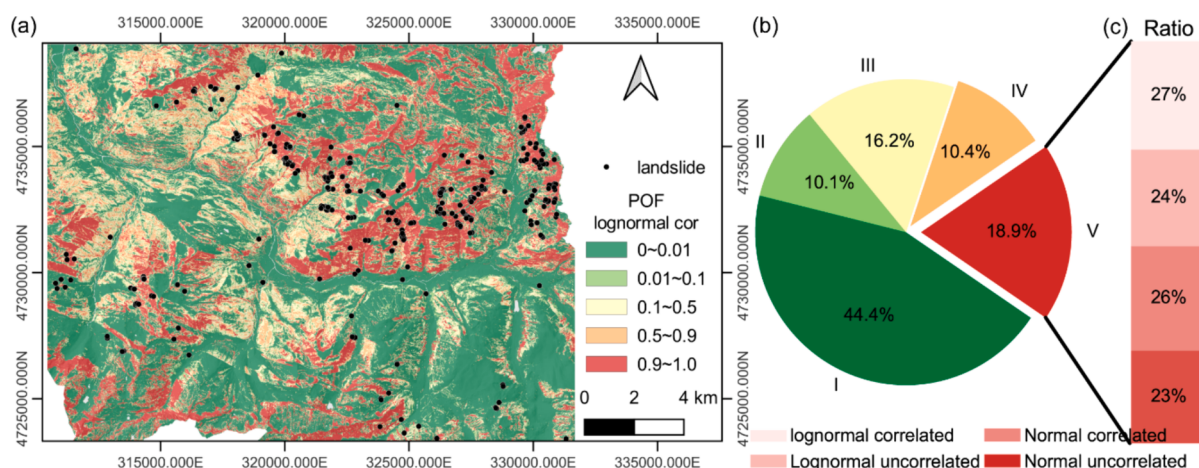


**Fig. 10.** Probabilistic landslide susceptibility analysis after effective antecedent recharge and event rainfall: (a) landslide susceptibility maps of parameters belong to lognormal correlated; (b) graph of the percentage of five different susceptibility levels after superimposition and normalisation for the four cases (parameter normal uncorrelated, normal correlated, lognormal uncorrelated, or lognormal correlate); (c) Proportions belonging to different distributions within the very high susceptibility classes, respectively.

**Table 6**

The frequency ratio considers cross-correlations under different hydrological conditions for different susceptibility levels.

Hydrological conditions	Susceptibility levels/ $\rho$	Percentage of landslide numbers (%)					Percentage of graded area (%)					Frequency ratio				
		0	-0.1	-0.3	-0.5	-0.7	0	-0.1	-0.3	-0.5	-0.7	0	-0.1	-0.3	-0.5	-0.7
$q_a$	I	43.9	44.5	45.9	47.9	51.0	7.2	6.6	14.1	20.2	51.9	0.16	0.54	0.83	1.84	3.23
	II	12.2	12.0	11.5	10.8	9.6	7.2	6.9	13.8	19.7	52.4	0.16	0.57	0.84	1.85	3.20
	III	16.9	16.5	15.5	14.3	12.3	8.2	6.6	13.0	17.4	54.7	0.18	0.58	0.84	1.73	3.22
	IV	11.0	10.7	10.0	9.2	8.1	9.2	6.6	12.0	14.3	57.8	0.19	0.62	0.84	1.56	3.24
	V	16.1	16.4	17.0	17.8	19.0	11.0	7.2	9.7	11.3	60.9	0.22	0.74	0.79	1.40	3.21
$q_a + P_e$	I	6.6	6.6	7.2	8.2	9.2	41.2	41.8	43.2	45.2	48.2	0.16	0.16	0.17	0.18	0.19
	II	4.9	4.9	5.4	5.9	6.4	12.2	12.0	11.5	10.7	9.6	0.40	0.41	0.47	0.55	0.66
	III	13.8	13.8	12.8	11.3	9.7	17.4	17.0	16.1	14.8	12.9	0.79	0.81	0.80	0.76	0.76
	IV	16.6	16.4	14.8	13.0	10.0	11.7	11.4	10.7	9.9	8.7	1.42	1.43	1.38	1.32	1.14
	V	58.1	58.3	59.8	61.6	64.7	17.5	17.9	18.5	19.4	20.5	3.31	3.27	3.23	3.19	3.15

potential for soil destabilization across various slope orientations. However, a detailed analysis will be performed to understand how antecedent recharge and event rainfall influence the probabilistic spatial distribution of landslides, particularly considering changes in the cross-negative correlation of parameters.

Therefore, the POF was extracted for landslide and non-landslide sites by considering different cross-negative correlations under different hydrological scenarios ( $q_a$  and  $q_a + P_e$ ). As illustrated in Fig. 12, notable variations in the failure probability of landslides primarily manifest within the high sensitivity range, while modifications in non-landslide areas predominantly occur within the low sensitivity range. However, it is noteworthy that as the negative correlation increases, the variation in non-landslide points near the low failure probability becomes more pronounced. For example, in the  $q_a + P_e$  case, the non-landslide points located in the very low damage probability interval (0–0.01) increased rapidly from 49.1 % to 55.3 %, while the landslide points located in the very high damage probability interval (0.9 to 1.0) increased from 15.3 % to 18.8 %. These results demonstrate that the FSLAM-FORM model effectively captures the effects of changes in parameter correlations on landslide and non-landslide sites at a regional scale.

Similar to the observed trend in COV variations, regions demonstrating high sensitivity are primarily concentrated within event rainfall ranges of 77–107 mm and 137–167 mm when accounting for parameter cross-negative correlations or non-normal distributions (as shown in Fig. 13). However, it is noteworthy that an increase in negative correlation coefficient, particularly when utilizing non-normally distributed parameters. This leads to a higher proportion of highly sensitive areas with event rainfall between 77–107 mm for antecedent rainfall of 0.5 mm/d. Specifically, as the negative correlation coefficient rises from 0.1 to 0.7, the corresponding ratio of V-class areas increases from 8.1 % to 9.1 %. For regions experiencing antecedent recharge of 0.1 mm/d and event rainfall ranging from 137 to 167 mm, the V-class area ratio escalates from 8.1 % to 9.7 %. In contrast, independent normal parameters yield a V-class area ratio of 8.1 %, whereas related lognormal parameters result in a V-class area ratio reaching 8.9 %.

#### 4.3.3. Combined comparison of spatial distribution probabilities for landslide impacts considering v statistical correlation and hydrological conditions

Variations in the cross-correlation coefficient are fundamentally connected to diverse failure mechanisms. This is evident as a decrease in this coefficient correlates with a heightened susceptibility to failure. Notably, a negative coefficient implies reduced cohesion, typically resulting in an increased angle of internal friction, and vice versa. When the negative correlation is substantial, it notably increases the uncertainty in soil shear parameters (Tang et al., 2013). This escalation leads to greater variability in total shear strength and a rise in the variance of slope stability (Griffiths et al., 2009). Consequently, the regions with the greatest susceptibility (characterised by the highest probability of failure) exhibit a broader spatial distribution. Moreover, it's important to

recognise that cross-correlation alone does not entirely represent the uncertainty in these variables. For a thorough assessment of uncertainty, cross-correlation should be examined in conjunction with the distribution function, which depends on the chosen form of parameter distribution. The failure probability is widely acknowledged to be determined by the integration of the joint probability distribution function (PDF) across all random variables within the failure region of the limit state function (Bhattacharyya, 2021). Therefore, various joint probability distributions can lead to different failure modes and significantly alter the POF. Selecting an appropriate distribution is critical for accurately conducting probabilistic analyses of landslide susceptibility.

In conclusion, these findings illustrate the significant impact of negative correlation among geotechnical parameters on evaluating the susceptibility of rainfall-triggered shallow landslides under different hydrological conditions. With the escalation of negative correlation, predictions regarding the distribution of landslides grow more uncertain, especially in situations involving event rainfall ( $P_e$ ). These outcomes highlight the importance of accounting for both the variability and the interrelationships of geotechnical parameters in regional assessments of landslide susceptibility.

#### 4.4. Assessment and analysis of modelling performance

##### 4.4.1. ROC analysis

The ROC curve is a highly significant and widely used method for evaluating model performance in prediction modelling, making it an essential tool in assessing the predictive capabilities of PBM models. Fig. 14 presents the ROC curves of various hydrological conditions investigated in this study, including results based on FS and POF. In terms of deterministic analysis (FS), the corresponding AUC values for dry conditions, saturated conditions, initial conditions (considering only antecedent recharge), as well as final conditions (after recharge and event rainfall) are 0.66, 0.70, 0.71, and 0.71 respectively. However, it is worth noting that the AUC values for the POF-based model in the aforementioned cases are 0.67, 0.73, 0.75, and 0.76 respectively. This observation indicates that the POF-based models consistently demonstrate superior predictive performance compared to their FS-based counterparts in our analysis. Furthermore, considering the event rainfall condition can significantly enhance the AUC value. Specifically, the AUC value increased to 0.76 when both antecedent recharge and event rainfall were taken into account. These findings emphasize the importance of considering the combined effect of antecedent and event rainfall when assessing landslide occurrences in the Val d'Aran area.

Furthermore, Table 7 presents additional performance metrics based on the confusion matrix for different hydrological conditions, utilising a POF threshold of 0.5 which was regarded as a. The model exhibits a high recall under the 'saturation condition', indicating its proficiency in accurately identifying most positive instances. However, this leads to an increased number of false positives and subsequently diminishes the corresponding F1 score, resulting in reduced precision. It is important to note that the F1 score represents a balanced average of both precision

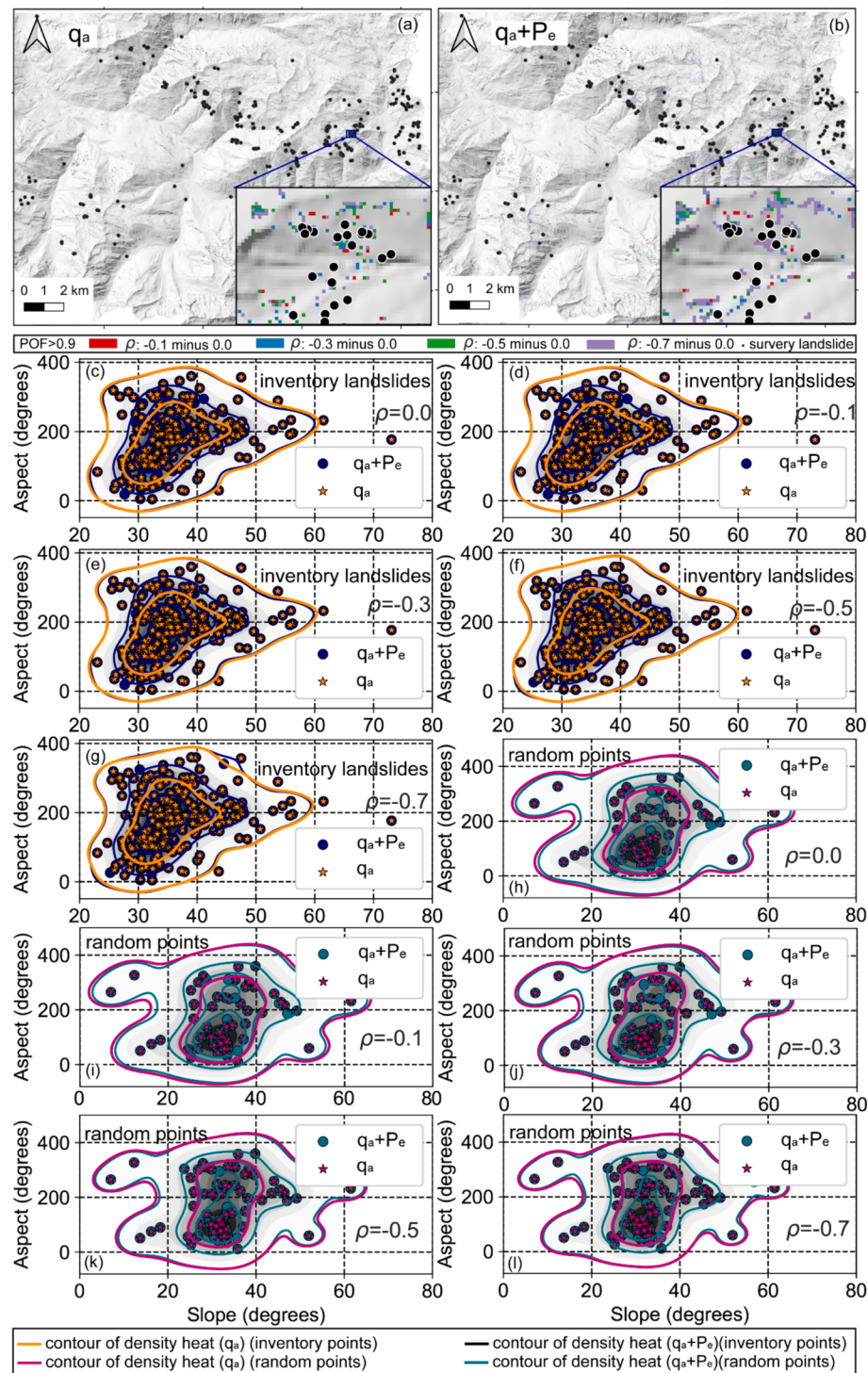


**Fig. 11.** (a) Impact of cross negative-correlation variations on the areas with very high susceptibility ( $POF > 0.9$  under different hydrological conditions ( $q_a$ ) and ( $q_a + P_e$ ). Kernel density estimation of areas of very high susceptibility under  $q_a$  and  $q_a + P_e$  conditions, segmented by slope and aspect: (c–g); random points (h–l).

and recall, making it particularly sensitive to lower values for both metrics. Therefore, optimal performance can be achieved by considering both antecedent recharge and event rainfall, resulting in an observed F1 score of 0.29. Furthermore, under dry conditions, the distance to perfect classification was 0.75 compared to a value of 0.37 under the  $q_a + P_e$  condition, thereby highlighting the crucial significance of incorporating both antecedent and event rainfall data. These indices collectively indicate that the FSLAM-FORM model effectively captures most landslide occurrences in the region while demonstrating commendable

performance results.

#### 4.4.2. Comparison of $AUC_{CDF}$ (area under the CDF curve) considering different probability scenarios

Notable disparities are observed in the variations of the cumulative distribution function (CDF) and probability of failure (POF) under different rainfall conditions. To assess stability, we calculated the area under the CDF curve ( $AUC_{CDF}$ ) (Hürlimann et al., 2022). A lower  $AUC_{CDF}$  value indicates greater instability within the study region.

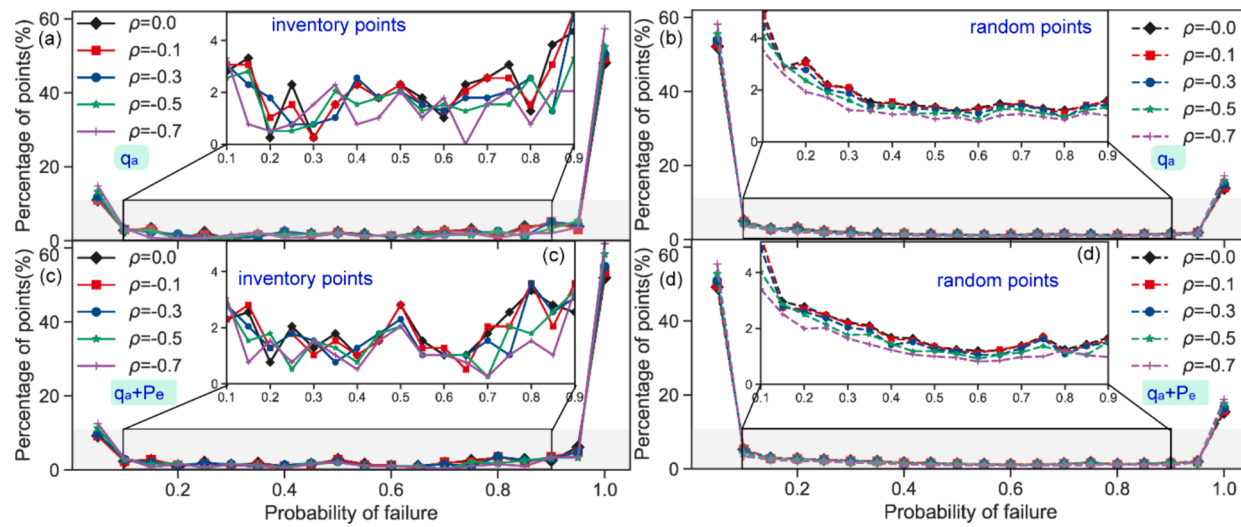


**Fig. 12.** Comparison between inventory points and random points under different rainfall conditions and cross-correlations: only antecedent rainfall for (a) inventory points; (b) random points; antecedent and event rainfall for (c) inventory points; (d) random points.

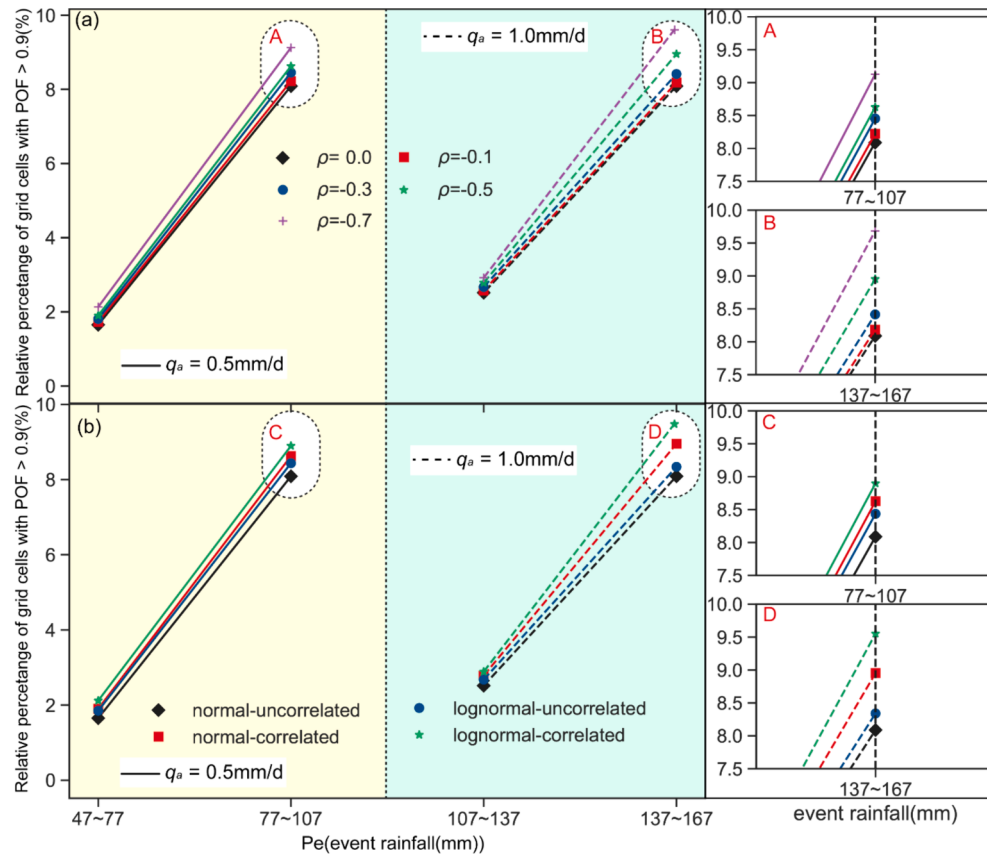


**Fig. 13.** Effect of the two rainfall inputs (antecedent ( $q_a$ ) and event rainfall ( $P_e$ )) on the percentage of very high susceptibility areas (POF > 0.9%): (a) different cross-correlation; (b) different statistical distribution.

Therefore, to comprehensively assess the predictive landslide susceptibility of GIS-FSLAM-FORM across various parameter variabilities, cross-correlation levels, and distribution conditions, we quantified the area under the  $AUC_{CDF}$  for each specific condition as shown in Fig. 15.

The CDF versus the probability of failure is depicted in Fig. 15a for various COV and cross-correlation values. With the COV increases, the correlation between the CDF and the POF becomes more distinct. This suggests that heightened system variability contributes to increased

instability in slope shear strength and a smaller stable region, thereby elevating the potential of landslides. The association between COV and  $AUC_{CDF}$  is illustrated in Fig. 15b, revealing a nearly linear decrease with a high accuracy of 99 %. This exhibits a discernible linear trend in parameter variability for the assessment of rainfall-induced landslide susceptibility. In Fig. 15c, negative cross-correlation is illustrated alongside  $AUC_{CDF}$ . A larger cross-correlation corresponds to higher  $AUC_{CDF}$  values. Unlike the linear effect observed with parameter

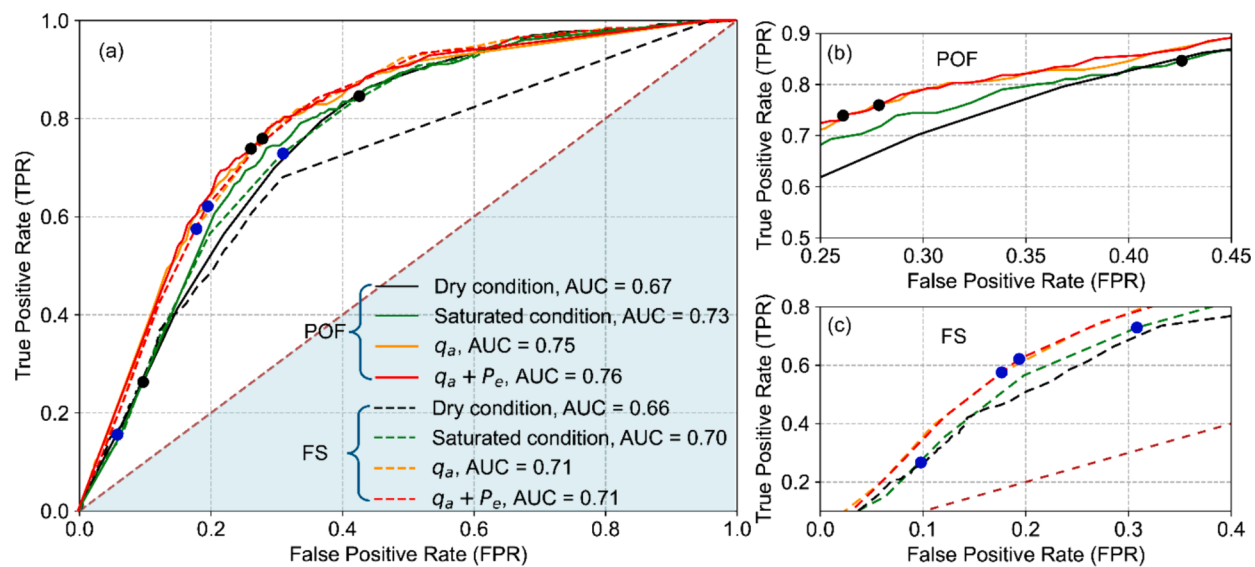


**Fig. 14.** Probabilistic results of adopting FSLAM-FORM method under dry conditions, totally saturated, after only  $q_a$ , and after  $q_a$  and  $P_e$ , respectively. (a) POF- and FS-based ROC curves with corresponding AUC values; (b) zoom-in of the POF results for the TPR range from 0.25 to 0.45; (c) zoom-in of the FS results for the TPR range from 0.0 to 0.4. The black or blue points in each curve show the corresponding FPR and TPR values when POF = 0.5. The distances from these points to the perfect classification are shown in Table 7. (For interpretation of the references to colour in this figure legend, the reader is referred to the web version of this article.)

**Table 7**

The confusion matrix when using the POF = 0.5 as the threshold of the safety level of slope stability.

Simulated cases	TP	TN	FP	FN	TPR	FPR	AUC	POD	ACC	BA	Precision	Recall	F1	r
Dry condition	101	4529	471	290	0.26	0.09	0.67	0.26	0.86	0.58	0.18	0.26	0.21	0.75
Saturated condition	327	2911	2089	64	0.84	0.42	0.73	0.84	0.60	0.71	0.14	0.84	0.23	0.45
$q_a$	283	3718	1282	108	0.72	0.26	0.75	0.72	0.74	0.73	0.18	0.72	0.29	0.38
$q_a + P_e$	293	3634	1366	98	0.75	0.27	0.76	0.75	0.73	0.74	0.18	0.75	0.29	0.37

r: Distance to perfect classification.

variability on  $AUC_{CDF}$ , negative parameter correlation tends to present non-linear behaviour and has an overall stronger impact than COV alone.

This indicates that stronger correlations among physical parameters contribute to increased landslide susceptibility. Fig. 15d. depicts the relationship between the CDF and the POF across various statistical distributions. For a normal distribution, the CDF-POF curve is comparatively smooth, while for a lognormal distribution, it demonstrates a more pronounced, steeper slope. This highlights the significance of selecting the appropriate parameter distribution type to improve the accuracy of predictions.

#### 4.4.3. Research limitations

Regarding the regions characterised by heightened non-normal parameter variability and more pronounced negative cross-correlation exhibit an elevated susceptibility to landslides. While this study primarily addresses the uncertainties associated with shear strength parameters, it is imperative to acknowledge the influence of spatial variability on physically-based susceptibility models and other geotechnical engineering concerns (Liu and Zhang, 2019; Luo et al., 2021). For instance, Burton et al. (1998) conducted a comprehensive investigation on the spatial variability of geotechnical parameters, such as cohesion, through extensive field measurements. Their findings revealed the significant influence of these parameters on landslide modelling. The consideration of spatial variability in geotechnical and hydrological parameters when assessing landslide susceptibility has been extensively investigated by numerous researchers (e.g., Yang et al. (2018); Mergili et al. (2014); Arnone et al. (2016)).

Therefore, it is crucial to consider the impact of spatially varying model parameters on the assessment of shallow landslide susceptibility

by incorporating the variability of these parameters at a spatial scale. This aspect holds significant potential for future research employing the FSLAM-FORM methodology. To enhance the accuracy and reliability of landslide susceptibility assessment in these areas with limited dataset, it is imperative to investigate the integration of real-time geo-monitoring and data analysis techniques, high-resolution remote-sensing data, geostatistical methods such as kriging, and machine learning algorithms for dynamically adjusting the parameters of the FSLAM-FORM model. This will significantly improve the robustness and predictive capability of input data.

## 5. Conclusion

Variations in slope materials and the scarcity of data contribute to uncertainties in regional geological parameters, which in turn significantly impact rainfall-induced shallow landslides in mountainous areas. To address this, we introduce a probabilistic analysis framework coupled with physically-based modelling, accompanied by the “Py.GIS-FSLAM-FORM” software. Our study comprehensively examines regional-scale shallow landslide susceptibility, taking into account parameter variability, cross-correlation, and statistical distribution scenarios under different hydrological conditions. The following conclusions are obtained:

- While physically-based models such as the FSLAM offer practical benefits, a common limitation in probabilistic models is their reliance on the assumption of independent normal distributions for parameters. This often leads to a neglect of the actual shapes of distributions and the inherent cross-correlations between parameters. This limitation is not exclusive to FSLAM but is prevalent in

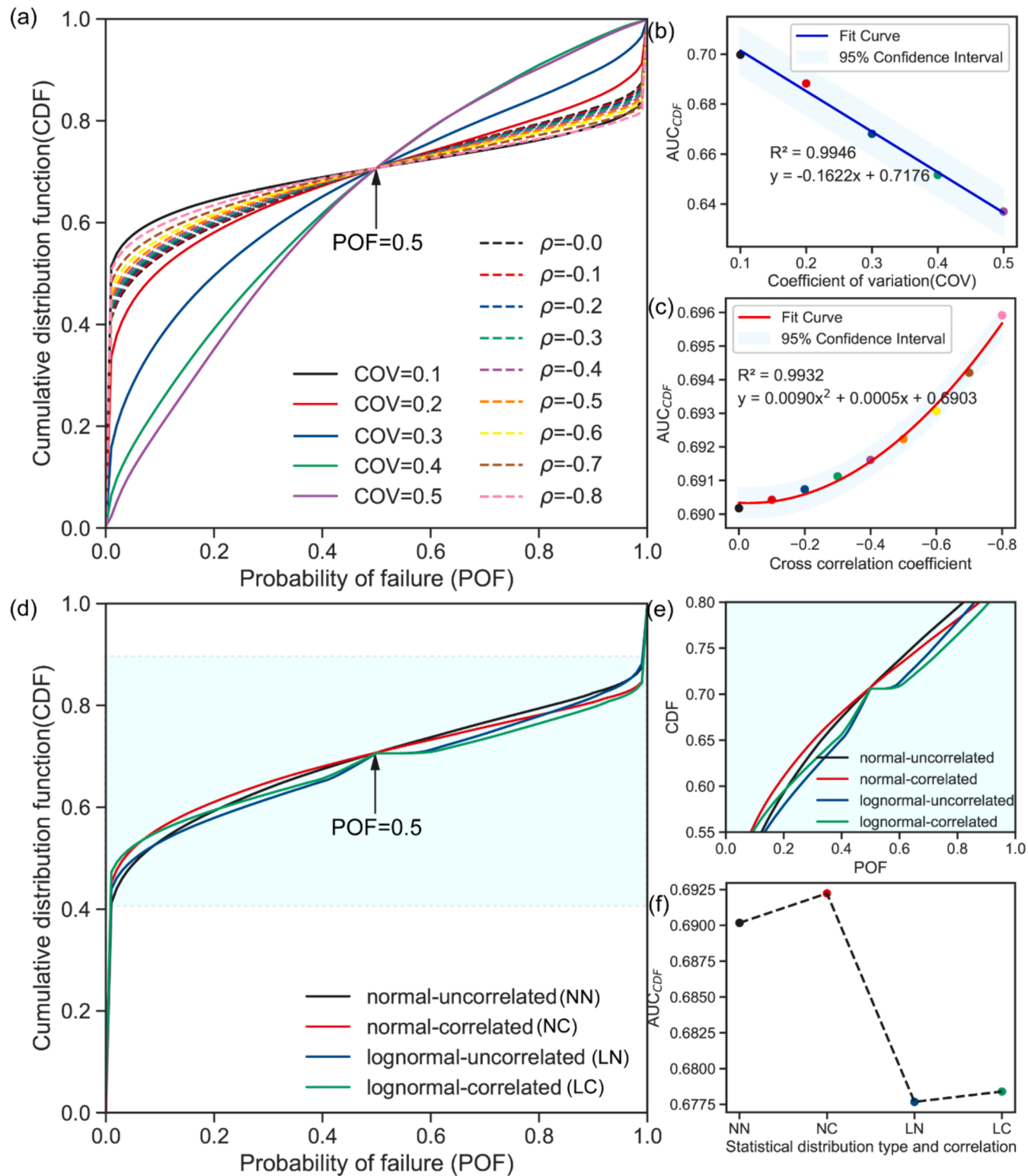


**Fig. 15.** The cumulative distribution function (CDF) versus POF after  $q_a$  and  $P_e$ : (a) different COVs and cross-correlations; the relationship between (b) COVs and  $AUC_{CDF}$ ; (c) cross-correlations and  $AUC_{CDF}$ ; (d) different statistical distributions; (e) local enlarge plot; (f) the relationship between and statistical distributions  $AUC_{CDF}$ .

various susceptibility models. To address these issues, our study introduces the first-order reliability method (FORM), thereby establishing a more robust and comprehensive probabilistic framework for efficient landslide susceptibility mapping.

- The results of the probabilistic analyses show that hydrological conditions significantly influence shallow landslide susceptibility,

especially the combined effect of effective antecedent recharge and event rainfall. The density heatmaps and contour analyses present that event rainfall expands the spatial distribution of highly susceptible areas under combined hydrological factors. The expansion is particularly evident in areas where slopes are between 30 and 40 degrees and where aspects range from 100 to 250 degrees.

- The variation in geotechnical parameters, particularly the coefficient of variation (COV) of cohesion and the internal friction angle plays a crucial role in assessing the susceptibility of rainfall-triggered shallow landslides. The application of our new probabilistic model reveals that an elevated COV significantly impacts the stability of landslide susceptibility predictions. The presence of a higher COV leads to an increased spatial dispersion in probabilistic landslide predictions, consequently amplifying the level of uncertainty. Additionally, regions typically classified as exhibiting extremely low or exceedingly high susceptibility are likely to transition towards a state of moderate or elevated susceptibility as the COV increases. This phenomenon becomes more pronounced under circumstances that combine effective antecedent recharge and event rainfall.
- The correlation between geotechnical parameters significantly influences the results of landslide susceptibility assessment, particularly the inverse relationship between cohesion and internal friction angle, as well as their non-normal distribution. The spatial distribution of landslide susceptibility undergoes significant changes with an increase in negative correlation, particularly during event rainfall. The variation becomes more pronounced as the negative correlation increases, especially when effective antecedent recharge and event rainfall jointly exert their influence. The spatial distribution of very high susceptibility in areas experiencing 77–107 mm of rainfall is significantly amplified by the heightened negative correlation, particularly when parameters deviate from a normal distribution. This underscores the compounded impact of cross-negative correlation and non-normal distributions on landslide susceptibility.

#### CRediT authorship contribution statement

**Hongzhi Cui:** Writing – review & editing, Writing – original draft, Visualization, Validation, Software, Methodology, Investigation, Formal analysis, Data curation, Conceptualization. **Vicente Medina:** Validation, Formal analysis, Conceptualization. **Marcel Hürliemann:** Writing – review & editing, Supervision, Methodology, Conceptualization. **Jian Ji:** Writing – review & editing, Validation, Supervision, Methodology, Conceptualization, Funding acquisition, Writing – original draft.

#### Declaration of competing interest

The authors declare that they have no known competing financial interests or personal relationships that could have appeared to influence the work reported in this paper.

#### Data availability

Data will be made available on request.

#### Acknowledgements

This work is financially supported by the National Natural Science Foundation of China (GRANT NOS: U22A20594, 52079045). Hongzhi Cui acknowledges the financial support of the China Scholarship Council (CSC: 202206710014) for his research at Universitat Politècnica de Catalunya.

#### References

- Abancó, C., Asurza, F.A., Medina, V., Hürliemann, M., Bennett, G.L., 2024. Modelling antecedent soil hydrological conditions to improve the prediction of landslide susceptibility in typhoon-prone regions. *Landslides*. <https://doi.org/10.1007/s10346-024-02242-8>.
- Aleotti, P., Chowdhury, R., 1999. Landslide hazard assessment: summary review and new perspectives. *Bull. Eng. Geol. Environ.* 58, 21–44. <https://doi.org/10.1007/s100640050066>.
- Arnone, E., Dialynas, Y.G., Noto, L.V., Bras, R.L., 2016. Accounting for soil parameter uncertainty in a physically based and distributed approach for rainfall-triggered landslides: Soil Parameter Uncertainty in Distributed Landslide Analysis. *Hydrology Processes*, 30, 927–944. <https://doi.org/10.1002/hyp.10609>.
- Baum, R.L., Savage, W.Z., Godt, J.W., 2008. TRIGRS: A Fortran Program for Transient Rainfall Infiltration and Grid-based Regional Slope-stability Analysis, version 2.0. US Geological Survey, Reston, VA, USA.
- Bhattacharyya, B., 2021. Structural reliability analysis by a Bayesian sparse polynomial chaos expansion. *Struct. Saf.* 90, 102074 <https://doi.org/10.1016/j.strusafe.2020.102074>.
- Bozzolan, E., Holcombe, E.A., Pianosi, F., Marchesini, I., Alvioli, M., Wagener, T., 2023. A mechanistic approach to include climate change and unplanned urban sprawl in landslide susceptibility maps. *Sci. Total Environ.* 858, 159412 <https://doi.org/10.1016/j.scitotenv.2022.159412>.
- Bui, D.T., Tuan, T.A., Klempé, H., Pradhan, B., Revhaug, I., 2016. Spatial prediction models for shallow landslide hazards: a comparative assessment of the efficacy of support vector machines, artificial neural networks, kernel logistic regression, and logistic model tree. *Landslides* 13, 361–378. <https://doi.org/10.1007/s10346-015-0557-6>.
- Burton, S., Lichtenstein, D.R., Netemeyer, R.G., Garretson, J.A., 1998. A scale for measuring attitude toward private label products and an examination of its psychological and behavioral correlates. *J. Acad. Mark. Sci.* 26, 293–306. <https://doi.org/10.1177/0092070398264003>.
- Carrara, A., Crosta, G., Frattini, P., 2008. Comparing models of debris-flow susceptibility in the alpine environment. *Geomorphology* 94, 353–378. <https://doi.org/10.1016/j.geomorph.2006.10.033>.
- Cepeda, J., Chávez, J.A., Cruz Martínez, C., 2010. Procedure for the selection of runout model parameters from landslide back-analyses: application to the Metropolitan Area of San Salvador, El Salvador. *Landslides* 7, 105–116. <https://doi.org/10.1007/s10346-010-0197-9>.
- Chen, G., Zhang, K., Wang, S., Xia, Y., Chao, L., 2023. iHydroSlide3D v1.0: an advanced hydrological-geotechnical model for hydrological simulation and three-dimensional landslide prediction. *Geosci. Model Dev.* 16, 2915–2937. <https://doi.org/10.5194/gmd-16-2915-2023>.
- Corominas, J., van Westen, C., Frattini, P., Cascini, L., Malet, J.-P., Fotopoulou, S., Catani, F., Van Den Eeckhaut, M., Mavrouli, O., Agliardi, F., Pitilakis, K., Winter, M. G., Pastor, M., Ferlisi, S., Tofani, V., Hervás, J., Smith, J.T., 2014. Recommendations for the quantitative analysis of landslide risk. *Bull. Eng. Geol. Environ.* 73, 209–263. <https://doi.org/10.1007/s10064-013-0538-8>.
- CREAF, 2020. The Land Cover Map of Catalonia.
- Cui, H., Ji, J., Hürliemann, M., Medina, V., 2024. Probabilistic and physically-based modelling of rainfall-induced landslide susceptibility using integrated GIS-FORM algorithm. *Landslides*. <https://doi.org/10.1007/s10346-024-02226-8>.
- Dolojan, N.L.J., Moriguchi, S., Hashimoto, M., Terada, K., 2021. Mapping method of rainfall-induced landslide hazards by infiltration and slope stability analysis. *Landslides* 18, 2039–2057. <https://doi.org/10.1007/s10346-020-01617-x>.
- Durmaz, M., Hürliemann, M., Huval, N., Medina, V., 2023. Comparison of different hydrological and stability assumptions for physically-based modeling of shallow landslides. *Eng. Geol.* 323, 107237 <https://doi.org/10.1016/j.enggeo.2023.107237>.
- Fuchs, M., Torizin, J., Kühn, F., 2014. The effect of DEM resolution on the computation of the factor of safety using an infinite slope model. *Geomorphology* 224, 16–26. <https://doi.org/10.1016/j.geomorph.2014.07.015>.
- Gorsevski, P.V., Gessler, P.E., Boll, J., Elliot, W.J., Foltz, R.B., 2006. Spatially and temporally distributed modeling of landslide susceptibility. *Geomorphology* 80, 178–198. <https://doi.org/10.1016/j.geomorph.2006.02.011>.
- Griffiths, D.V., Huang, J., Fenton, G.A., 2009. Influence of spatial variability on slope reliability using 2-D random fields. *J. Geotech. Geoenviron. Eng.* 135, 1367–1378. [https://doi.org/10.1061/\(ASCE\)GT.1943-5606.0000099](https://doi.org/10.1061/(ASCE)GT.1943-5606.0000099).
- Gupta, K., Satyam, N., Gupta, V., 2023. Probabilistic physical modelling and prediction of regional seismic landslide hazard in Uttarakhand state (India). *Landslides* 20, 901–912. <https://doi.org/10.1007/s10346-022-02013-3>.
- Ho, J.-Y., Lee, K.T., 2016. Performance evaluation of a physically based model for shallow landslide prediction. *Landslides* 14, 961–980. <https://doi.org/10.1007/s10346-016-0762-y>.
- Huang, F., Xiong, H., Yao, C., Catani, F., Zhou, C., Huang, J., 2023. Uncertainties of landslide susceptibility prediction considering different landslide types. *J. Rock Mech. Geotech. Eng.* <https://doi.org/10.1016/j.jrmge.2023.03.001>.
- Hürliemann, M., Guo, Z., Puig-Polo, C., Medina, V., 2022. Impacts of future climate and land cover changes on landslide susceptibility: regional scale modelling in the Val d’Aran region (Pyrenees, Spain). *Landslides* 19, 99–118. <https://doi.org/10.1007/s10346-021-01775-6>.
- Hwang, I.-T., Park, H.-J., Lee, J.-H., 2023. Probabilistic analysis of rainfall-induced shallow landslide susceptibility using a physically based model and the bootstrap method. *Landslides* 20, 829–844. <https://doi.org/10.1007/s10346-022-02014-2>.
- ICGC, 2013. Terrain Elevation Model of Catalonia 5×5 meters. Last accessed 11 May 2021. <https://www.icgc.cat/appdownloads/>.
- ICGC, 2016. Geological map 1:50000. Last accessed 11 May 2021. <https://www.icgc.cat/Administracio-i-empresa/Descarregues/Cartografia-geologica-i-geomatica/Cartografia-geologica/Mapa-geologic-comarcal-1-50.000>.
- Javankhoshsedel, S., Bathurst, R.J., 2016. Influence of cross correlation between soil parameters on probability of failure of simple cohesive and c-φ slopes. *Can. Geotech. J.* 53, 839–853. <https://doi.org/10.1139/cgj-2015-0109>.
- Ji, J., Cui, H., Zhang, T., Song, J., Gao, Y., 2022. A GIS-based tool for probabilistic physical modelling and prediction of landslides: GIS-FORM landslide susceptibility analysis in seismic areas. *Landslides* 19, 1–19. <https://doi.org/10.1007/s10346-022-01885-9>.

- Ji, J., Kodikara, J.K., 2015. Efficient reliability method for implicit limit state surface with correlated non-Gaussian variables. *Int. J. Numer. Anal. Meth. Geomech.* 39, 1898–1911. <https://doi.org/10.1002/nag.2380>.
- Ji, J., Zhang, C., Gao, Y., Kodikara, J., 2019. Reliability-based design for geotechnical engineering: an inverse FORM approach for practice. *Comput. Geotech.* 111, 22–29. <https://doi.org/10.1016/j.comgeo.2019.02.027>.
- Jiang, Y., Hu, X., Liang, H., Ning, P., Fan, X., 2023. A physically based model for the sequential evolution analysis of rainfall-induced shallow landslides in a catchment. *Water Resour. Res.* 59, e2022WR032716 <https://doi.org/10.1029/2022WR032716>.
- Lacasse, S., Nadim, F., 2011. Learning to live with geohazards: from research to practice. Presented at the Georisik 2011. [https://doi.org/10.1061/41183\(418\).4](https://doi.org/10.1061/41183(418).4).
- Lambe, T., Whitman, R., 1979. *Soil Mechanics*. John Wiley & Sons Inc, New York, NY, USA.
- Li, C., Guo, C., Yang, X., Li, H., Zhou, J., 2022. A GIS-based probabilistic analysis model for rainfall-induced shallow landslides in mountainous areas. *Environ. Earth Sci.* 81, 18. <https://doi.org/10.1007/s12665-022-10562-y>.
- Liu, C.-N., Wu, C.-C., 2008. Mapping susceptibility of rainfall-triggered shallow landslides using a probabilistic approach. *Environ. Geol.* 55, 907–915. <https://doi.org/10.1007/s00254-007-1042-x>.
- Liu, Y., Zhang, L., 2019. Seismic response of pile-raft system embedded in spatially random clay. *Géotechnique* 69, 638–645. <https://doi.org/10.1680/jgeot.17.T.015>.
- Liu, Y., Zhang, W., Zhang, L., Zhu, Z., Hu, J., Wei, H., 2018. Probabilistic stability analyses of undrained slopes by 3D random fields and finite element methods. *Geosci. Front.* 9, 1657–1664. <https://doi.org/10.1016/j.gsf.2017.09.003>.
- Low, B.K., Phoon, K.-K., 2015. Reliability-based design and its complementary role to Eurocode 7 design approach. *Comput. Geotech.* 65, 30–44. <https://doi.org/10.1016/j.comgeo.2014.11.011>.
- Low, B., Tang, W.H., 2007. Efficient spreadsheet algorithm for first-order reliability method. *J. Eng. Mech.* 133, 1378–1387. [https://doi.org/10.1061/\(ASCE\)0733-9399\(2007\)133:12\(1378\)](https://doi.org/10.1061/(ASCE)0733-9399(2007)133:12(1378)).
- Luo, J., Zhang, L., Yang, H., Wei, X., Liu, D., Xu, J., 2021. Probabilistic model calibration of spatial variability for physically-based landslide susceptibility model. *Georisik: Assess. Manag. Risk Eng. Syst. Geohazards* 16, 1–18. <https://doi.org/10.1080/17499518.2021.1988986>.
- Ma, G., Rezania, M., Mousavi Nezhad, M., Hu, X., 2022. Uncertainty quantification of landslide runout motion considering soil interdependent anisotropy and fabric orientation. *Landslides* 19, 1231–1247. <https://doi.org/10.1007/s10346-021-01795-2>.
- Marin, R.J., Mattos, Á.J., 2020. Physically-based landslide susceptibility analysis using Monte Carlo simulation in a tropical mountain basin. *Georisik: Assess. Manag. Risk Eng. Syst. Geohazards* 14, 192–205. <https://doi.org/10.1080/17499518.2019.1633582>.
- Medina, V., Hürlimann, M., Guo, Z., Lloret, A., Vaunat, J., 2021. Fast physically-based model for rainfall-induced landslide susceptibility assessment at regional scale. *Catena* 201, 105213. <https://doi.org/10.1016/j.catena.2021.105213>.
- Meisina, C., Scarabelli, S., 2007. A comparative analysis of terrain stability models for predicting shallow landslides in colluvial soils. *Geomorphology, Stud. Weather. Slope Movements* 87, 207–223. <https://doi.org/10.1016/j.geomorph.2006.03.039>.
- Mergili, M., Marchesini, I., Rossi, M., Guzzetti, F., Fellin, W., 2014. Spatially distributed three-dimensional slope stability modelling in a raster GIS. *Geomorphology* 206, 178–195. <https://doi.org/10.1016/j.geomorph.2013.10.008>.
- Mondini, A., Guzzetti, F., Melillo, M., 2023. Deep learning forecast of rainfall-induced shallow landslides. *Nat. Commun.* 14, 2466. <https://doi.org/10.1038/s41467-023-38135-y>.
- Montgomery, D.R., Dietrich, W.E., 1994. A physically based model for the topographic control on shallow landsliding. *Water Resour. Res.* 30, 1153–1171. <https://doi.org/10.1029/93WR02979>.
- Montrasio, L., Valentino, R., 2008. A model for triggering mechanisms of shallow landslides. *Nat. Hazard. Earth Sys.* 8, 1149–1159. <https://doi.org/10.5194/nhess-8-1149-2008>.
- Oguz, E.A., Depina, I., Thakur, V., 2022. Effects of soil heterogeneity on susceptibility of shallow landslides. *Landslides* 19, 67–83. <https://doi.org/10.1007/s10346-021-01738-x>.
- Pack, R.T., Tarboton, D.G., Goodwin, C.N., 1998. The SINMAP approach to terrain stability mapping. *Eng. Geol. Nat. Hazards* 2, 1157–1165.
- Park, H., Jang, J., Lee, J., 2019. Assessment of rainfall-induced landslide susceptibility at the regional scale using a physically based model and fuzzy-based Monte Carlo simulation. *Landslides* 16, 695–713. <https://doi.org/10.1007/s10346-018-01125-z>.
- Pradhan, B., 2013. A comparative study on the predictive ability of the decision tree, support vector machine and neuro-fuzzy models in landslide susceptibility mapping using GIS. *Comput. Geosci.* 51, 350–365. <https://doi.org/10.1016/j.cageo.2012.08.023>.
- Raia, S., Alvioli, M., Rossi, M., Baum, R.L., Godt, J.W., Guzzetti, F., 2014. Improving predictive power of physically based rainfall-induced shallow landslide models: a probabilistic approach. *Geosci. Model Dev.* 7, 495–514. <https://doi.org/10.5194/gmd-7-495-2014>.
- Raimondi, L., Pepe, G., Firpo, M., Calcaterra, D., Cevasco, A., 2023. An open-source and QGIS-integrated physically based model for Spatial Prediction of Rainfall-Induced Shallow Landslides (SPRIn-SL). *Environ. Model. Softw.* 160 <https://doi.org/10.1016/j.envsoft.2022.105587>.
- Segoni, S., Rossi, G., Catani, F., 2012. Improving basin scale shallow landslide modelling using reliable soil thickness maps. *Nat. Hazards* 61, 85–101. <https://doi.org/10.1007/s11069-011-9770-3>.
- Shinoda, M., Miyata, Y., Kurokawa, U., Kondo, K., 2019. Regional landslide susceptibility following the 2016 Kumamoto earthquake using back-calculated geomaterial strength parameters. *Landslides* 16, 1497–1516. <https://doi.org/10.1007/s10346-019-01171-1>.
- Shu, H., Hurlmann, M., Molowny-Horas, R., Gonzalez, M., Pinyol, J., Abanco, C., Ma, J., 2019. Relation between land cover and landslide susceptibility in Val d'Arán, Pyrenees (Spain): historical aspects, present situation and forward prediction. *Sci. Total Environ.* 693, 133557 <https://doi.org/10.1016/j.scitotenv.2019.07.363>.
- Tandjiria, V., Teh, C.I., Low, B.K., 2000. Reliability analysis of laterally loaded piles using response surface methods. *Struct. Saf.* 22, 335–355. [https://doi.org/10.1016/s0167-4730\(00\)00019-9](https://doi.org/10.1016/s0167-4730(00)00019-9).
- Tang, X.-S., Li, D.-Q., Rong, G., Phoon, K.-K., Zhou, C.-B., 2013. Impact of copula selection on geotechnical reliability under incomplete probability information. *Comput. Geotech.* 49, 264–278. <https://doi.org/10.1016/j.comgeo.2012.12.002>.
- Tao, Y., Phoon, K.-K., Sun, H., Cai, Y., 2023. Hierarchical Bayesian model for predicting small-strain stiffness of sand. *Can. Geotech. J.*
- Tran, T.V., Alvioli, M., Lee, G., An, H.U., 2018. Three-dimensional, time-dependent modeling of rainfall-induced landslides over a digital landscape: a case study. *Landslides* 15, 1071–1084. <https://doi.org/10.1007/s10346-017-0931-7>.
- USDA, S., 1986. *Urban hydrology for small watersheds. Technical release 55*, 2–6.
- USDA, S., 2007. National Engineering Handbook: Part 630 - Chapter 7: Hydrologic Soil Groups. National Resources Conservation Service.
- Wang, M., Tang, X., Li, D., Qi, X., 2020. Subset simulation for efficient slope reliability analysis involving copula-based cross-correlated random fields. *Comput. Geotech.* 118, 103326 <https://doi.org/10.1016/j.comgeo.2019.103326>.
- Wang, L., Xiao, T., Liu, S., Zhang, W., Yang, B., Chen, L., 2023. Quantification of model uncertainty and variability for landslide displacement prediction based on Monte Carlo simulation. *Gondwana Res. Data driven models* 123, 27–40. <https://doi.org/10.1016/j.jgr.2023.03.006>.
- Wei, X., Zhang, L., Luo, J., Liu, D., 2021. A hybrid framework integrating physical model and convolutional neural network for regional landslide susceptibility mapping. *Nat. Hazards* 109, 471–497. <https://doi.org/10.1007/s11069-021-04844-0>.
- Weidner, L., Oomen, T., Escobar-Wolf, R., Sajinkumar, K.S., Samuel, R.A., 2018. Regional-scale back-analysis using TRIGRS: an approach to advance landslide hazard modeling and prediction in sparse data regions. *Landslides* 15, 2343–2356. <https://doi.org/10.1007/s10346-018-1044-7>.
- Yang, H.-Q., Zhang, L., Li, D.-Q., 2018. Efficient method for probabilistic estimation of spatially varied hydraulic properties in a soil slope based on field responses: a Bayesian approach. *Comput. Geotech.* 102, 262–272. <https://doi.org/10.1016/j.comgeo.2017.11.012>.
- Yi, Y., Zhang, Z., Zhang, W., Jia, H., Zhang, J., 2020. Landslide susceptibility mapping using multiscale sampling strategy and convolutional neural network: a case study in Jiuzhaigou region. *Catena* 195, 104851. <https://doi.org/10.1016/j.catena.2020.104851>.
- Yuan, K., Cheng, X., Gui, Z., Li, F., Wu, H., 2019. A quad-tree-based fast and adaptive Kernel Density Estimation algorithm for heat-map generation. *Int. J. Geogr. Inf. Sci.* 33, 2455–2476. <https://doi.org/10.1080/13658816.2018.1555831>.
- Zhang, J., Huang, H.W., Zhang, L.M., Zhu, H.H., Shi, B., 2014. Probabilistic prediction of rainfall-induced slope failure using a mechanics-based model. *Eng. Geol.* 168, 129–140. <https://doi.org/10.1016/j.enggeo.2013.11.005>.
- Zhang, L., Li, J., Li, X., Zhang, J., Zhu, H., 2016. *Rainfall-Induced Soil Slope Failure: Stability Analysis and Probabilistic Assessment*. Taylor & Francis Group, Florida.
- Zieher, T., Schneider-Muntau, B., Mergili, M., 2017. Are real-world shallow landslides reproducible by physically-based models? Four test cases in the Laternser valley, Vorarlberg (Austria). *Landslides* 14, 2009–2023. <https://doi.org/10.1007/s10346-017-0840-9>.